Multi-epoch hard X-ray view of Compton-thick AGN Circinus Galaxy

Abhijit Kayal [ID],[1,2]* Veeresh Singh [ID],[1] Claudio Ricci [ID],[3,4] N. P. S. Mithun [ID],[1] Santosh Vadawale [ID],[1] Gulab Dewangan [ID],[5] Poshak Gandhi [ID],[6]

[1] *Physical Research Laboratory, Navrangpura, Ahmedabad, Gujarat-380 009, India*
[2] *Indian Institute of Technology Gandhinagar, Palaj, Gandhinagar, Gujarat-382 355, India*
[3] *Núcleo de Astronomía de la Facultad de Ingeniería, Universidad Diego Portales, Av. Ejército Libertador 441, Santiago, Chile*
[4] *Kavli Institute for Astronomy and Astrophysics, Peking University, Beijing 100871, China*
[5] *Inter-University Centre for Astronomy and Astrophysics (IUCAA), SPPU Campus, 411007, Pune, India*
[6] *School of Physics & Astronomy, University of Southampton, Highfield, Southampton SO17 1BJ, UK*

ABSTRACT

The circumnuclear material around Active Galactic Nuclei (AGN) is one of the essential components of the obscuration-based unification model. However, our understanding of the circumnuclear material in terms of its geometrical shape, structure and its dependence on accretion rate is still debated. In this paper, we present the multi-epoch broadband X-ray spectral modelling of a nearby Compton-thick AGN in Circinus galaxy. We utilise all the available hard X-ray (> 10 keV) observations taken from different telescopes, i.e., *BeppoSAX*, *Suzaku*, *NuSTAR* and *AstroSat*, at ten different epochs across 22 years from 1998 to 2020. The $3.0-79$ keV broadband X-ray spectral modelling using physically-motivated models, namely MYTORUS, BORUS02 and UXCLUMPY, infers the presence of a torus with a low covering factor of 0.28, an inclination angle of $77° - 81°$ and Compton-thick line-of-sight column densities ($N_{\rm H,LOS} = 4.13 - 9.26 \times 10^{24}$ cm^{-2}) in all the epochs. The joint multi-epoch spectral modelling suggests that the overall structure of the torus is likely to remain unchanged. However, we find tentative evidence for the variable line-of-sight column density on timescales ranging from one day to one week to a few years, suggesting a clumpy circumnuclear material located at sub-parsec to tens of parsec scales.

Key words: galaxies: active — galaxies: Seyfert — galaxies: individual: Circinus — X-rays: galaxies — methods: observational

1 INTRODUCTION

The widely accepted unification model of Active Galactic Nuclei (AGN) invokes a gaseous and dusty axisymmetric toroidal structure popularly known as 'torus' around the accreting Super-Massive Black Holes (SMBHs) (e.g., Antonucci & Miller 1985; Urry & Padovani 1995; Ramos Almeida & Ricci 2017). Based on the orientation of the obscuring torus, AGN can be classified mainly into two sub-classes named as type 1 (pole-on view) and type 2 (edge-on view). The evidence for the presence of the obscuring torus has come from a variety of observations that include the detection of broad emission lines in spectro-polarimetric observations of type 2 Seyferts (Moran 2007), biconical shapes of narrow-line regions (NLRs) in type 2 Seyferts (Schmitt et al. 2003), and systematically higher X-ray absorbing column density in type 2 Seyferts (Singh et al. 2011; Ricci et al. 2017a). To explain the observed differences between two sub-classes of Seyfert galaxies, most of the early studies assumed a doughnut-shaped

uniform-density obscuring medium (see Netzer 2015). Albeit, X-ray monitoring campaigns of nearby AGN (e.g., NGC 1365; Risaliti et al. 2005, NGC 4151; Puccetti et al. 2007, and NGC 7582; Rivers et al. 2015) finding the change in absorbing column density on timescales of days to several hours, favoured a clumpy obscuring medium. The discrete clouds forming the obscuring medium possibly exist at scales ranging from sub-parsec to a few hundred parsecs (Bianchi et al. 2012; Torricelli-Ciamponi et al. 2014). Also, the column density of clumpy absorbing medium is likely to increase towards the equatorial plane (see Nenkova et al. 2008). However, despite a large number of studies, the location, geometry, and physical state of the obscuring material are still widely debated (e.g., Hönig 2019; Saha et al. 2022).

The high−resolution infrared (IR) observations from the Very Large Telescope Interferometer (VLTI) have revealed that, contrary to the prevalent paradigm of the classical torus, the dust around AGN is not distributed in one single toroidal structure (Hönig et al. 2012; Tristram et al. 2014; Leftley et al. 2018). In fact, a two-component structure composed of an equatorial thin disk and a polar-extended cone-like fea-

ture, is implied from the modelling of IR interferometry data. However, IR observations probe only the dusty phase of the obscuring matter around the AGN and may not yield a complete picture of circumnuclear material. The X-ray observations of AGN can provide insights into the geometry and distribution of circumnuclear material owing to the fact that X-ray emission emanating from the inner regions of the accreting system carries imprints of absorption and scattering caused by the gaseous phase of circumnuclear material (Risaliti et al. 2005; Morgan et al. 2012).

The multi-epoch X-ray observations have revealed a significant change in the line-of-sight column density ($N_{\rm H,LOS}$) even in Compton-thick ($N_{\rm H,LOS} > 1.5 \times 10^{24}$ cm^2) AGN (CT−AGN) (e.g., MRK 3; Guainazzi et al. 2016, NGC 1068; Zaino et al. 2020, NGC 1358; Marchesi et al. 2022). The timescale for a significant variability in $N_{\rm H,LOS}$ depends on the distances, velocities and filling factors of the obscuring clouds around the SMBH. The type 2 AGN, in which line-of-sight passes through the obscuring torus, can be suitable targets to probe changes in $N_{\rm H,LOS}$ (Ricci & Trakhtenbrot 2022). However, only a small number of such sources have been studied, hitherto, due to the unavailability of multi-epoch hard X-ray observations on timescales ranging from a few days to years. The hard X-ray (> 10 keV) observations are crucial to probe any variation in the covering factor and to break well-known line-of-sight column density and photon index ($N_{\rm H,LOS} - \Gamma$) degeneracy (see Puccetti et al. 2014; Marchesi et al. 2019). Also, hard X-ray observations are useful in mitigating the influences of off-nuclear X-ray sources. With the availability of multi-epoch hard X-ray observations on timescales ranging from days to years, Circinus galaxy (hereafter 'Circinus') is a suitable target for investigating changes associated with the AGN and reprocessing circumnuclear material. Due to its proximity (redshift (z) 0.00145±0.00001 and luminosity distance (D$_{\rm L}$) 4.2±0.8 Mpc; Freeman et al. (1977)) and brightness, Circinus offers an advantage for performing an in-depth study of circumnuclear reprocessing material.

In this paper, we investigate changes associated with the circumnuclear X-ray reprocessing material such as $N_{\rm H,LOS}$, average column density and covering factor in Circinus, for the first time, using multi-epoch hard X-ray observations from the *BeppoSAX*, *Suzaku*, Nuclear Spectroscopic Telescope Array (*NuSTAR*), and *AstroSat* taken at ten different epochs across the period of 22 years from 1998 to 2020. The hard X-ray observations of the last three epochs i.e., 2016 August 23, 2020 January 28 and 2020 November 26, are presented here for the first time. The paper is organized as follows. In Section 2, we provide a brief description of previous studies performed on Circinus with the main focus on the results obtained from the hard X-ray observations. In Section 3, we give the details of X-ray observations and data reduction. In Section 4, we present the X-ray spectral modelling of off-nuclear sources and contamination model. In Section 5, we describe multi-epoch broadband X-ray modelling. Section 6 is devoted to the discussion of plausible geometry, changes in line-of-sight column density and the location of obscuring clouds. In Section 7, we summarise the results of our study.

In our paper, we assume a flat Λ-cold dark matter cosmology with H$_0$ = 70 km s^{-1} Mpc^{-1}, Ω_Λ = 0.73, and $\Omega_{\rm m}$ = 0.27, the same as those used in XSPEC 12.11.1c (Arnaud 1996). With these cosmological parameters, $1''.0$ corresponds to 29 parsec at the distance of Circinus. We used Galactic neutral

column density of $N_{\rm H}^{\rm gal} = 5.6 \times 10^{21}$ cm^{-2} (Kalberla et al. 2005) toward the direction of Circinus. The errors quoted on the spectral parameters are of 90 per cent confidence, unless stated otherwise.

2 PREVIOUS STUDIES ON CIRCINUS

Based on the optical spectroscopic observations, Circinus is classified as a Seyfert type 2 AGN with starburst activity (Freeman et al. 1977; For et al. 2012). The mass of SMBH ($M_{\rm BH}$) in the Circinus is estimated to be 1.7×10^6 $M_\odot$ (Koss et al. 2017) using the relationship between black hole mass and stellar velocity dispersion (Kormendy & Ho 2013). The bolometric luminosity is estimated to be $L_{\rm bol} = 4 \times 10^{43}$ erg s^{-1} from the mid-IR (MIR) nuclear spectrum (Moorwood et al. 1996). The estimates of black hole mass and bolometric luminosity suggest an Eddington ratio ($L/L_{\rm Edd}$) of 0.2. The high−resolution VLTI mid-infrared interferometric instrument (MIDI) observations revealed that the parsec-scale MIR emission around the AGN in the Circinus is composed of two distinct components : (i) a disc-like component coinciding with the disc observed in maser emission, and (ii) a component extending in a polar direction, along the ionisation cone seen in the optical (Tristram et al. 2007, 2014). The polar component is found to be responsible for up to $\sim 80\%$ of the MIR emission on parsec-scales (Tristram et al. 2014).

Circinus is widely studied in the X-ray wavelengths and is classified as a CT−AGN. The X-ray observations below 10 keV from the *ASCA*, *Chandra*, and *XMM-Newton* showed only a reflection-dominated spectrum with a prominent Fe Kα emission line (see Matt et al. 1996; Guainazzi et al. 1999; Marinucci et al. 2013). Early observations at hard X-ray from the *BeppoSAX* showed a high absorbing column density of $N_{\rm H}$ $\sim 4 \times 10^{24}$ cm^{-2}, confirming Circinus to be a CT-AGN. Interestingly, two *BeppoSAX* observations performed almost three years apart during 1998 and 2001 reported a dramatic flux ($\sim$ 50 per cent) and spectral variation (Bianchi et al. 2002). The observed variability was ascribed to an extremely variable ultra−luminous X-ray (ULX) source named Circinus Galaxy X1(CGX1; Bauer et al. 2001) that contaminated *BeppoSAX* spectrum obtained with $2'.0$ extraction region. However, an intrinsic variation in AGN flux or line-of-sight column density could not be completely ruled out. Using 3−70 keV *Suzaku* observations, Yang et al. (2009) reported the presence of a direct AGN component transmitted through a column density of $\simeq 4 \times 10^{24}$ cm^{-2}. Later on, using *Chandra* and *XMM-Newton* observations of higher spatial resolution Arévalo et al. (2014) accounted for the contribution from the off-nuclear contaminating X-ray sources, and reported that the hard X-ray spectrum is Compton-scattered by an optically-thick torus having equatorial column density $6 - 10 \times 10^{24}$ cm^{-2} with a relatively steeper photon index of $\Gamma = 2.2 - 2.4$. Notably, *NuSTAR* observations did not support the detection of transmitted AGN component, which was earlier suggested with the *Suzaku* observations. More recently, Andonie et al. (2022) showed that the 3−70 keV *NuSTAR* spectrum of Circinus could also be fitted with a model considering the reprocessing components consisted of an accretion disc, BLR, a flared disc and a hollow cone in the polar direction.

3 X-RAY OBSERVATIONS AND DATA REDUCTION

For our study, we utilised all the available hard X-ray observations ($E > 10$ keV) taken from various telescopes (e.g., *BeppoSAX, Suzaku NuSTAR* and *AstroSat*) during 1998 to 2020. Circinus is observed with the *NuSTAR* at six different epochs, twice with the *BeppoSAX*, and once each with the *AstroSat* and *Suzaku*. To assess the contamination from the off-nuclear X-ray sources, we utilised *Chandra* and *XMM-Newton* observations. The *XMM-Newton* observations taken on 2013 February 03 and 2016 August 23 were performed quasi−simultaneously with the *NuSTAR* observations of corresponding epochs. The start and end times of each *XMM-Newton* and *NuSTAR* pair of observations are within 12 hours. We list the basic details of all the X-ray observations in Table 1. In the following subsections, we describe our observations and data reduction procedures.

3.1 *NuSTAR*

Circinus has been observed with the *NuSTAR* (Harrison et al. 2013) with its two co-aligned units having focal plane modules FPMA and FPMB. We note that all the *NuSTAR* observations, except one taken on 2013 January 25 have targeted an ULX binary named ULX5 (see Mondal et al. 2021) residing $4'$ to the south−west of the AGN, thus imaged Circinus at off-axis. The *NuSTAR* with $12'.5 \times 12'.5$ field-of-view (FOV) and angular resolutions of $18''$ Full Width at Half Maximum (FWHM) offers a clear detection of Circinus, along with the ULX5.

The *NuSTAR* data were reduced using the standard pipeline (NUPIPELINE) provided in the *NuSTAR* Data Analysis Software (NUSTARDAS, v2.1.2) within the HEASoft package (v6.30), in combination with the calibration database (v20220706). The unfiltered level 1 event lists were screened to reduce the internal background at high energies via standard depth corrections and removal of South Atlantic Anomaly (SAA) passages. The latest calibration files were used to create level 2 event files. We extracted the source spectra and lightcurves of AGN by using an aperture with a radius of $100''$ for both FPMA and FPMB. The background spectra were extracted from a source-free region in the same chip using a circular aperture of the same size. We note that the 2016 *NuSTAR* observations show Circinus at a large off-axis angle of $5'.7$ with an elongated PSF. Hence, to include all the source emission with minimum contamination from the background, we extracted the source spectrum from an elliptical region (major axis = $90''$, minor axis = $50''$ and PA = $44°$). The net exposure times and count rates for both FPMA and FPMB of our observations are listed in Table 1. To apply χ^2 statistics, we binned our spectra to have a minimum of $50−100$ counts per bin.

3.2 *XMM-Newton*

To study the broadband spectral properties of Circinus, we used *XMM-Newton* observations taken simultaneously with the *NuSTAR* observations on 2013 February 03 and 2016 August 23, respectively (see Table 1). Both of these observations were aimed at ULX5. The AGN located nearly $4'$ away is well detected due to sufficiently high angular resolution ($6''.0$) and large FOV ($30'$) of EPIC pn/MOS cameras. Also, to check variability in off-nuclear sources, we used *XMM-Newton* observations taken on four different epochs, *i.e,* 2018 September 18, 2016 August 23, 2013 February 03 and 2001 August 06. During all the epochs, EPIC pn observations were taken in the full window mode with the medium filter, except for 2016 when the thin filter was used.

We reduced the data using Science Analysis System (SAS v19.0.0) following the standard procedure. We considered only single and double events with quality flag set equal to 0. We obtained calibrated event files by using the latest calibration files. The good time interval event files were generated by removing time intervals of flaring background with count rates exceeding 0.8 ct s^{-1} for pn in the $10−12$ keV band. The net exposure times for pn in the $0.5−10$ keV energy band are found to be 85.5 ks, 16.2 ks, 36.2 ks and 103.0 ks for 2018, 2016, 2013 and 2001 observations, respectively (see Table 1). We generated response matrices and ancillary response files using the rmfgen and arfgen tasks, respectively. The spectra were binned to have a minimum of 30 counts per bin.

To perform the joint *XMM-Newton* and *NuSTAR* spectral fit, we extracted the *XMM-Newton* pn spectrum using $100''$ radius to match the extraction region of the *NuSTAR* spectrum. The background spectra were extracted using a polygon region covering an area devoid of any source emission in the same chip. We point out that the EPIC pn image, with an angular resolution of $6''.0$, enables us to spatially resolve AGN and neighbouring off-nuclear X-ray sources CGX1 and CGX2. We extracted CGX1 and CGX2 spectra using circular apertures of radii $7''.5$ and $11''$, respectively.

3.3 *AstroSat*

We (PI: A. Kayal) observed Circinus using *AstroSat* during 2020 January 28 to 2020 February 01. The Soft X-ray Telescope (SXT) onboard *AstroSat* was kept as the prime instrument for these observations.

3.3.1 *SXT*

The SXT, a grazing incidence X-ray telescope operating in 0.3–7.1 keV band, offers an angular resolution of $2'.0$ (Singh et al. 2017). The SXT observations of Circinus were performed in photon counting (PC) mode. We reduced data using SXTPIPELINE (version 1.4b[1]), and generated cleaned and calibrated level 2 event files for each orbit. The data reduction pipeline includes standard processes such as event extraction, screening criteria (e.g., eliminating bad pixels, SAA passage, and events with grades >12), and calibration. The cleaned and calibrated level 2 event files for each orbit were then merged using SXTPYJULIAMERGER_v02 that removed any overlap between the consecutive orbits. The merged level 2 event file gives an effective exposure time of 57.49 ks. The scientific data products, e.g., images, light curves and spectra, were extracted using the XSELECT task within the HEASoft package. We extracted the source spectrum using a circular region of radius $13'$ with encircled energy fraction of 92.3%. For spectral analysis, we used the SXT spectrum along with the relevant response files and background spectrum provided

---

[1] https://www.tifr.res.in/ astrosat_sxt/sxtpipeline.html

Table 1. Summary of X-ray observations used in this work

Epoch	Instrument	Date & start time	ObsID	Energy band (keV)	Detector	$T_{\rm exp}$ (ks)	Count-rate (cts s^{-1})	Off-axis ($'$)
(1)	(2)	(3)	(4)	(5)	(6)	(7)	(8)	(9)
1	NuSTAR	2020-11-26T05:51:09	80601502001	3−79	FPMA	106.1	0.86±0.01	2.65
				3−79	FPMB	105.2	0.82±0.01	2.65
2	AstroSat	2020-01-28T21:34:57	A07_100T02_9000003470 A07_100T02_9000003476	0.3−7.0	SXT	57.5	0.13±0.01	0.06
				3−80	LAXPC	85.4	6.72±0.10	0.06
				22−70	CZTI	71.0	0.56±0.06	...
	XMM Newton	2018-09-18T13:48:49	0824450301	0.5−10	pn	85.5	1.09±0.01	6.04
3	NuSTAR	2016-08-23T06:41:08	90201034002	3−79	FPMA	49.8	0.57±0.01	5.76
				3−79	FPMB	49.7	0.55±0.01	5.76
	XMM Newton	2016-08-23T16:53:33	0792382701	0.5−10	pn	16.2	1.72±0.01	5.78
4	NuSTAR	2013-02-05T05:06:07	30002038006	3−79	FPMA	36.2	0.82±0.01	3.05
				3−79	FPMB	36.1	0.85±0.01	3.05
5	NuSTAR	2013-02-03T03:01:07	30002038004	3−79	FPMA	40.3	0.84±0.01	2.91
				3−79	FPMB	40.2	0.86±0.01	2.91
	XMM Newton	2013-02-03T07:24:11	0701981001	0.5−10	pn	36.2	1.89±0.01	3.69
6	NuSTAR	2013-02-02T01:01:07	30002038002	3−79	FPMA	18.3	0.92±0.01	2.85
				3−79	FPMB	18.3	0.92±0.01	2.85
7	NuSTAR	2013-01-25T03:51:07	60002039002	3−79	FPMA	53.9	1.12±0.01	2.73
				3−79	FPMB	53.8	1.05±0.01	2.73
	Chandra	2010-12-17T18:10:27	12823	0.5−10	ACIS-S	152.4	0.06±0.01	0.21
8	Suzaku	2006-07-21T12:29:57	701036010	0.5−10	XIS-0	108.0	0.54±0.01	0.93
				0.5−10	XIS-1	108.0	0.53±0.01	0.76
				0.5−10	XIS-2	108.0	0.53±0.01	0.97
				0.5−10	XIS-3	108.0	0.52±0.01	1.09
				10−70	HXD-PIN	88.3	0.40±0.01	3.91
				50−120	HXD-GSO	88.3	0.14±0.01	3.91
9	BeppoSAX	2001-01-07T06:36:41	5114000100	2.0−10	MECS	51.7	0.18±0.01	1.77
				15−100	PDS	37.9	1.72±0.03	...
	XMM-Newton	2001-08-06T08:54:51	0111240101	0.5−10	pn	103.0	2.45±0.01	1.71
10	BeppoSAX	1998-03-13T06:32:49	5004700200	2.0−10	MECS	71.5	0.14±0.01	1.88
				15−100	PDS	63.3	1.83±0.03	...

Notes - $T_{\rm exp}$ is the net exposure time after removal of bad time−intervals. The net count rate in the total energy band is estimated after the removal of bad time−intervals and subtraction of background. The parameters of *AstroSat* observations are combination of observations taken under the two different observation IDs. Epochs are listed in chronological order based on the availability of hard X-ray (> 10 keV) observations.

by the SXT instrument team. Considering calibration uncertainties in the response, we added a systematic uncertainty of 3 per cent to the SXT data (e.g., Jithesh et al. 2019; Swain et al. 2023). To account for the slight change in the SXT gain (Singh et al. 2017) we used gain fit task in the XSPEC by fixing the slope to 1 keV and varying the offset parameter. Subsequently, we fixed the offset parameter to the resultant value of 0.03 keV.

3.3.2 LAXPC

The LAXPC, sensitive in the 3.0–80 keV band, is a non-focusing instrument (Antia et al. 2017). The *AstroSat* houses three identical units of proportional counters (LAXPC10, LAXPC20 and LAXPC30), filled with highly pressurised xenon gas. The LAXPC30 unit is suspected to have undergone a gas leakage resulting in a continuous gain shift and LAXPC10 is unstable (see Antia et al. 2017). Hence, we used data from the LAXPC20 unit only. The data from LAXPC were processed and analysed using the latest version (August 15, 2022) of the LAXPC pipeline package `laxpcSoft`, pro-

vided by the LAXPC POC[2]. The level 2 event file was generated by combining the level 1 event files from all orbits and removing any overlap between two consecutive orbits. We obtain a net exposure time of 85.4 ks by considering only good time intervals and selecting events from only the top layer of the LAXPC20 unit. The spectrum and lightcurve were extracted from the level 2 file by applying appropriate response functions and gain variations. We applied gain shift utility to account for the shift in gain values of the background spectrum during the time of observations. We obtained a gain offset of −0.4 keV, a value similar to the one reported in previous studies (see Antia et al. 2021). Due to the completely background−dominated spectrum at higher energies, we used the LAXPC spectrum only in the 4−20 keV energy band. We also added systematic uncertainty of 3.0 per cent to account for calibration uncertainties in the response (see Antia et al. 2021).

[2] https://www.tifr.res.in/astrosat_laxpc/software.html

3.3.3 CZTI

The Cadmium Zinc Telluride Imager (CZTI, Bhalerao et al. 2017) onboard *AstroSat* is a hard X-ray coded mask instrument operating in the $22-200$ keV energy range. It contains four identical but independent quadrants, with each quadrant consists of sixteen CZT detector modules. We reduced data using CZTI data analysis pipeline[3] version 3.0. From the raw event list, we generated cleaned event files by applying the recommended good time interval (GTI) selection criteria. We generated background subtracted spectra for each quadrant by using the `cztbindata` task. The spectra of all four quadrants from two sets of observations (A07_100T02_9000003470 and A07_100T02_9000003476) were added together by using the `cztaddspec` task. The combination of two observations provided a net exposure time of 71.0 ks. The source counts were detected above 5σ in the $22-70$ keV energy range. Hence, we used the $22-70$ keV CZTI spectrum after grouping it into broader energy bins.

3.4 Suzaku

The Circinus was observed with the *Suzaku* (Mitsuda et al. 2007) on 2006 July 21, for nearly 140 ks. There are four X-ray Imaging Spectrometer (XIS, Koyama et al. 2007) CCDs located at the focal planes of the respective foil mirrors X-ray telescopes, and a non-imaging collimated Hard X-ray Detector (HXD) onboard *Suzaku*. The four XIS CCDs, i.e., XIS0, XIS1, XIS2, and XIS3 are sensitive in $0.4-10$ keV energy band. The three XIS units have front-illuminated CCDs, while XIS1 with back-illuminated CCDs provides better quantum efficiency in the sub-keV energy range. The HXD uses 16 phoswich counter detectors, with each unit consisting of a GSO scintillation counter and PIN silicon diodes. The PIN detector is sensitive in the energy range of $12-60$ keV, while GSO is sensitive above 40 keV.

We reduced the XIS and HXD data using the HEASoft software package (version 6.30) and following the steps given in Suzaku Data Reduction Guide[4]. From cleaned calibrated event files, we extracted XIS spectra using a circular extraction region with a radius of $2'.5$ centered at the Circinus. The background spectra were extracted from a source-free region. The HXD spectra were generated using the `HXD-PINXBPI` script. The HXD being a collimating instrument, requires background estimation from the non-X-ray instrumental background (NXB) and cosmic X-ray background (CXB). We utilised the response and NXB files provided by the Suzaku team. To apply χ^2 minimisation, we binned PIN and GSO spectra such that each bin has a minimum signal-to-noise ratio of 3. The binned spectra of PIN and GSO have energy ranges of $10-70$ keV and $50-120$ keV, respectively. The count rates for PIN and GSO are 0.40 ± 0.01 ct s^{-1} and 0.14 ± 0.01 ct s^{-1}, respectively. We note that, due to relatively coarse angular resolution, both XIS as well as HXD spectra of Circinus are contaminated by the neighbouring off-nuclear sources.

3.5 BeppoSAX

The X-ray satellite *BeppoSAX* (Boella et al. 1997) carried four co-aligned instruments, namely a Low Energy Concentrator Spectrometer (LECS), three Medium Energy Concentrator Spectrometers (MECS), a High-Pressure Gas Scintillation Proportional Counter (HPGSPC), and a Phoswich Detector System (PDS). With imaging capabilities, LECS and MECS operated in $0.1-10$ keV and $1.3-10$ keV energy ranges, respectively and both have an angular resolution of nearly $1'.2$ arcmin at 6 keV. The HPGSPC and PDS are collimating instruments and cover $4-120$ keV and $15-200$ keV energy ranges, respectively. Since PDS is more sensitive than HPGSPC in the overlapping energy range, we preferred to use PDS data. Also, considering the better sensitivity of MECS than LECS in the overlapping band, we used the MECS spectrum. Thus, our broadband spectral analysis is based on MECS and PDS spectra. We obtained MECS and PDS spectral products from the SSDC multi-mission interactive archive[5]. The corresponding response and background files were taken from the CALDB directory.

3.6 Chandra ACIS-S

The high spatial resolution ($0''.5$) of *Chandra* ACIS-S enables us to resolve and assess the contribution of off-nuclear sources (see Figure 1). To perform spectral analysis of off-nuclear sources and extended diffuse emission, we used *Chandra* ACIS-S observations of Circinus taken on 17 December 2010 (see Section 4). With 152 ks exposure time, these are the deepest imaging observations performed with the *Chandra*. The ACIS-S, sensitive in the $0.4-8.0$ keV energy range, consists of four front-illuminated and two back-illuminated CCDs. We reduced *Chandra* data using the CIAO software[6] (v4.14) and the latest available calibration files from CALDB v4.9.8. In data processing, we removed $0''.5$ pixel randomization, and corrected for charge transfer inefficiency (CTI), excluded bad pixels and time intervals of high background. With a 3.2s frame time, no source except AGN suffers from the pile-up. Using calibrated and cleaned event file, we extracted spectra of off-nuclear sources.

4 ASSESSMENT OF CONTAMINATION FROM OFF-NUCLEAR SOURCES

We point out that *Chandra* ACIS and *XMM-Newton* pn images offering higher angular resolutions of $0''.5$ and $6''.0$, respectively, show off-nuclear X-ray sources CGX1 and CGX2 located close to the AGN (see Figure 1). CGX1 is located north-east to the AGN at a distance of $15''$, while CGX2 is detected at a distance of $25''$ towards the south of AGN. The *NuSTAR* images with an angular resolution of $18''$ (FWHM) are unable to spatially resolve CGX1 and CGX2. Therefore, the *NuSTAR* spectrum includes contributions from these two neighbouring off-nuclear X-ray sources in addition to that from AGN. We note that the deep *Chandra* ACIS image taken in 2010 December shows several faint off-nuclear sources in addition to CGX1 and CGX2. Although, Arévalo

---

[3] http://astrosat-ssc.iucaa.in/cztiData
[4] https://heasarc.gsfc.nasa.gov/docs/suzaku/analysis/abc/
[5] https://www.ssdc.asi.it/mmia/index.php?mission=saxnfi
[6] https://cxc.harvard.edu/ciao/
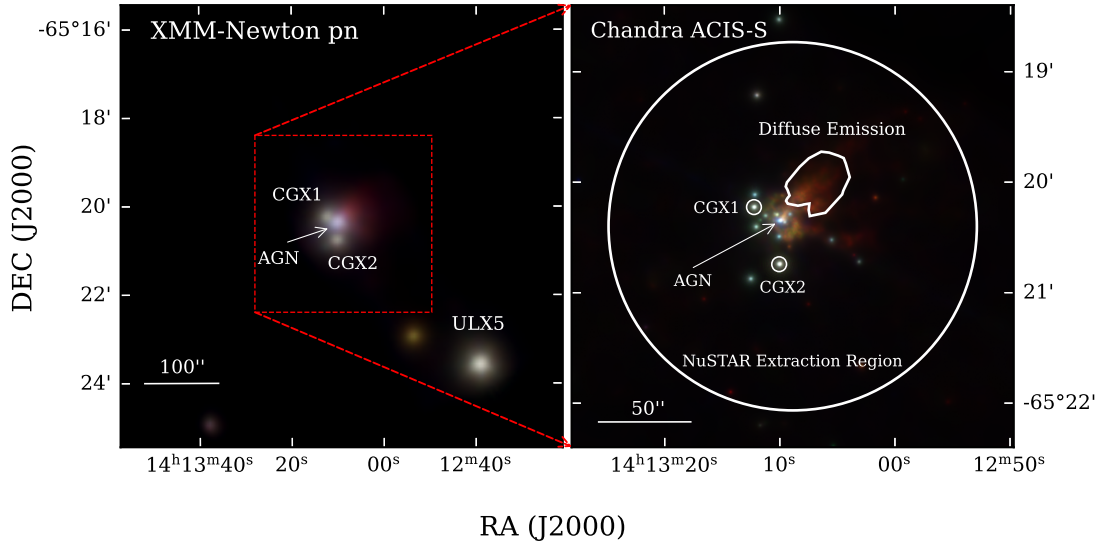
Figure 1. *Left panel*: The *XMM-Newton* pn image of Circinus in which the AGN and the off-nuclear contaminating sources CGX1, CGX2 and ULX5 are marked. *Right panel*: The zoom-in view of the central region as seen in the sensitive *Chandra* ACIS-S image of higher resolution obtained from the longest exposure time of 152 ks. The extraction regions of CGX1, CGX2 and extended diffuse emission, are marked. The location of the AGN is indicated by an arrow. The large circle represents the *NuSTAR* extraction region of 100″ radius. Three different colours in both images represent three different energy bands i.e., 0.3−1.5 keV (red), 1.5−2.5 keV (green) and 2.5−8.0 keV (blue).

et al. (2014) demonstrated that the cumulative contribution from the faint sources is insignificant in comparison to the CGX1 and CGX2, which is further vindicated by the fact that the *XMM-Newton* pn images of different epochs detect only relatively bright CGX1 and CGX2. Hence, we account for the contamination from CGX1 and CGX2 while analysing the *NuSTAR* spectra. We recall that the *XMM-Newton* and *NuSTAR* images show ULX5 (Walton et al. 2013) as a bright X-ray source located 4′.5 away south-west to the AGN. The *BeppoSAX*, *Suzaku* and *AstroSat* observations with a fairly coarse angular resolution of collimating instruments are unable to resolve AGN and neighbouring sources CGX1, CGX2 as well as ULX5. Except for *Suzaku* XISs spectra, the soft X-ray spectra from *BeppoSAX* MECS and *AstroSat* SXT include the contribution from the ULX5. Therefore, while modelling the broadband spectra of these instruments, we account for the contamination from the ULX5 too, in addition to the CGX1 and CGX2.

To assess and remove the contribution of contaminating off-nuclear X-ray sources, we followed a procedure similar to that presented by Arévalo et al. (2014). Using *Chandra* ACIS and *XMM-Newton* pn observations, we model 0.5−10 keV X-ray spectra of individual contaminants, i.e., CGX1, CGX2, ULX5 and extended emission. For each contaminating source, we attempt to achieve a baseline model that can provide a reasonably good fit to the spectra of all epochs. With the knowledge of the spectral shape and parameters of contaminants, we formulate a contamination model that accounts for the contribution of all contaminants. In the following subsections, we discuss spectral modelling of the contaminating sources and formulation of the contamination model.

4.1 CGX1

CGX1 is an X-ray binary classified as an ULX with $L_{0.3-8.0\ \text{keV}}$ in the range of 4.0×10^{39} erg s^{-1} to 3.0×10^{40} erg s^{-1} (Bauer et al. 2001; Esposito et al. 2015; Qiu et al. 2019). The *Chandra* ACIS and *XMM-Newton* pn/MOS images detect CGX1 at RA = $14^h\ 13^m\ 12.21^s$, DEC = -65° 20′ 13″.7 (J2000), which is 15″ away from the AGN toward the northeast. The *Chandra* ACIS observations of higher angular resolution (0″.5) offer a clean detection of CGX1 with no contamination from the AGN and the diffuse emission. We extracted the *Chandra* ACIS spectrum of CGX1 using a circular aperture of 2″.4 radius. Unlike *Chandra*, *XMM-Newton* pn spectra of CGX1 are extracted using a larger circular region of 7″.5 radius due to its larger PSF of 6″.0. Also, background determination in the *XMM-Newton* pn images is a little tricky due to the contamination from the AGN and the diffuse X-ray emission present around it. Following Arévalo et al. (2014), we extracted the background spectra for CGX1 using an annular region around it, which excludes masked circular regions around the neighbouring CGX2 and AGN. The inner and outer radii of the annular region were set as 7″.5 and 30″, respectively.

The *XMM-Newton* pn spectra begin to show rising background contamination above 6.0 keV (see Qiu et al. 2019). Therefore, we fit *XMM-Newton* pn spectra only in the 0.5−6.0 keV energy band. However, due to its higher angular resolution (0″.5) *Chandra* ACIS observations are not contaminated by the diffuse emission, and we consider the full 0.5−10 keV energy band, while fitting the *Chandra* spectrum. We find that the 0.5−10 keV *Chandra* spectrum can be best−fitted with a simple absorbed power law model with photon index (Γ) of 1.8. The absorption consists of two components, i.e., galactic column density fixed to 5.6×10^{21} cm^{-2} and in-

Table 2. The best−fitted spectral parameters and fluxes of CGX1, CGX2 and ULX5 during different epochs

Parameters	Unit	2001	2010	2013	2016	2018
(1)	(2)	(3)	(4)	(5)	(6)	(7)
CGX1 [Model: TBABS × TBABS × PO]						
$N_{\rm H}^{\rm gal}$	10^{22} cm^{-2}	0.56^f	0.56^f	0.56^f	0.56^f	0.56^f
$N_{\rm H}$	10^{22} cm^{-2}	$0.69^{+0.03}_{-0.03}$	$0.51^{+0.05}_{-0.05}$	$0.32^{+0.04}_{-0.04}$	$0.42^{+0.06}_{-0.06}$	$0.35^{+0.05}_{-0.05}$
Γ		1.8^f	$1.80^{+0.06}_{-0.06}$	1.8^f	1.8^f	1.8^f
$Norm_\Gamma$	10^{-4}	$1.10^{+0.22}_{-0.22}$	$2.48^{+0.21}_{-0.19}$	$3.96^{+0.16}_{-0.16}$	$5.98^{+0.30}_{-0.30}$	$1.87^{+0.08}_{-0.08}$
$F_{0.5-10.0\ \rm keV}$	10^{-12} erg cm^{-2} s^{-1}	$3.86^{+0.06}_{-0.06}$	$0.97^{+0.03}_{-0.03}$	$1.50^{+0.05}_{-0.05}$	$2.21^{+0.10}_{-0.10}$	$0.70^{+0.26}_{-0.28}$
$\chi_{\rm r}^2$ (dof)		1.28 (647)	1.09 (299)	1.06 (191)	0.69 (116)	1.11 (202)
CGX2 [Model: TBABS × (TBABS × VPSHOCK + TBABS × VPSHOCK)]						
$N_{\rm H}^{\rm gal}$	10^{22} cm^{-2}	0.56^f	0.56^f	0.56^f	0.56^f	0.56^f
$N_{\rm H}$	10^{22} cm^{-2}	$0.70^{+0.08}_{-0.08}$	$0.44^{+0.04}_{-0.04}$	$0.30^{+0.10}_{-0.09}$	$0.35^{+0.18}_{-0.19}$	$0.23^{+0.08}_{-0.08}$
$kT^{\rm R}$	keV	8.0^f	8.0^f	$7.89^{+0.75}_{-0.69}$	8.0^f	8.0^f
$kT^{\rm F}$	keV	3.0^f	3.0^f	$2.98^{+1.81}_{-0.87}$	3.0^f	3.0^f
$\tau_{\rm u}^{\rm R}$	10^{13} s cm^{-3}	5.0^f	5.0^f	$5.00^{\rm peg}_{-4.58}$	5.0^f	5.0^f
$\tau_{\rm u}^{\rm F}$	10^{11} s cm^{-3}	5.5^f	5.5^f	$5.50^{+7.01}_{-2.47}$	5.5^f	5.5^f
$Norm^{\rm R}$	10^{-4}	$6.81^{+0.40}_{-0.41}$	$7.13^{+0.33}_{-0.34}$	$5.98^{+0.65}_{-0.91}$	$4.88^{+0.65}_{-0.70}$	$4.16^{+0.25}_{-0.26}$
$Norm^{\rm F}$	10^{-4}	$3.34^{+0.70}_{-0.68}$	$2.96^{+0.47}_{-0.46}$	$2.15^{+0.86}_{-0.77}$	$0.99^{+1.03}_{-0.90}$	$0.64^{+0.37}_{-0.33}$
$F_{0.5-10\ \rm keV}$	10^{-12} erg cm^{-2} s^{-1}	$1.49^{+0.04}_{-0.04}$	$1.59^{+0.03}_{-0.03}$	$1.34^{+0.04}_{-0.04}$	$1.00^{+0.08}_{-0.08}$	$0.85^{+0.03}_{-0.03}$
$\chi_{\rm r}^2$ (dof)		0.96(472)	1.23 (338)	0.95(264)	1.26 (87)	1.13 (358)
ULX5 [Model: TBABS × DISKBB]						
$N_{\rm H}^{\rm gal}$	10^{22} cm^{-2}	0.56^f		0.56^f	0.56^f	0.56^f
$T_{\rm in}$	keV	$1.17^{+0.03}_{-0.03}$		$1.85^{+0.02}_{-0.02}$	$1.08^{+0.03}_{-0.03}$	$1.78^{+0.01}_{-0.01}$
$Norm_{\rm diskbb}$	10^{-2}	$2.37^{+0.27}_{-0.24}$		$3.26^{+0.16}_{-0.15}$	$8.88^{+0.10}_{-0.10}$	$3.53^{+0.11}_{-0.10}$
$F_{0.5-10.0\ \rm keV}$	10^{-12} erg cm^{-2} s^{-1}	$0.63^{+0.01}_{-0.02}$		$6.07^{+0.07}_{-0.08}$	$1.66^{+0.04}_{-0.06}$	$5.88^{+0.04}_{-0.05}$
$\chi_{\rm r}^2$ (dof)		1.75 (288)		0.97 (896)	1.06 (205)	1.13 (1198)
Diffuse emission [Model: TBABS × APEC + MYTORUS]						
$N_{\rm H}^{\rm gal}$	10^{22} cm^{-2}		0.56^f			
kT	keV		$0.82^{+0.02}_{-0.02}$			
Z	$Z_\odot$		$0.19^{+0.02}_{-0.02}$			
$Norm_{\rm apec}$	10^{-3}		$1.13^{+0.10}_{-0.09}$			
$N_{\rm H}$	10^{24} cm^{-2}		$10.00^{\rm peg}_{-4.08}$			
Γ			2.00^f			
$\theta_{\rm Incl}$	degrees		80^f			
$A_{\rm S}$	10^{-2}		$6.31^{\rm peg}_{-0.39}$			
$F_{0.5-10\ \rm keV}$	10^{-13} erg cm^{-2} s^{-1}		$8.85^{+0.15}_{-0.16}$			
$\chi_{\rm r}^2$ (dof)			1.15 (200)			

Notes - 2010 epoch observations are from *Chandra* ACIS-S while remaining are from *XMM-Newton* EPIC pn. $N_{\rm H}^{\rm gal}$ and $N_{\rm H}$ represent the Galactic and line-of-sight column density at the source redshift, respectively. Γ is photon index of power law emission. kT denotes plasma temperature. $\tau_{\rm u}$ represents the upper limit on the ionisation timescale in VPSHOCK model. 'R' and 'F' denote reverse and forward shock components, respectively. $A_{\rm S}$ is the normalisation of scattered component in MYTORUS model.
^{f} Fixed value for a parameter.

trinsic absorption due to the interstellar material (ISM) of the host galaxy. Notably, the *XMM-Newton* pn spectra for all four epochs can also be fitted with an absorbed power law (see Table 2). To attain a baseline model, we fixed the photon index to 1.8 while fitting the *XMM-Newton* spectra of different epochs. The absorbing column density and normalisations were left to vary. We find that absorbing column density is similar, in the range of $0.32^{+0.04}_{-0.04} \times 10^{22}$ cm^{-2} to $0.42^{+0.06}_{-0.06} \times 10^{22}$ cm^{-2}, during 2013, 2016 and 2018, while it is relatively high ($0.69^{+0.03}_{-0.03} \times 10^{22}$ cm^{-2}) in 2001 epoch. Our spectral fits of CGX1 are consistent with the fact that the change in flux is due to variable absorption rather than

the intrinsic change in the source itself (Qiu et al. 2019). We point out that the fitting of the 2001 spectrum can be improved (i.e., the reduce χ^2 changes from 1.28 to 1.11) by adding an ionised absorber (`absori`). However, the addition of the ionised absorber gives no significant improvement in the statistical fit of other epochs. Therefore, to maintain a simple common baseline model across all the epochs, we prefer to use only neutral absorbing material. Figure 2 shows the fitted spectra and residuals for all five different epochs. In Table 2, we list the best−fitted parameters for different epochs.
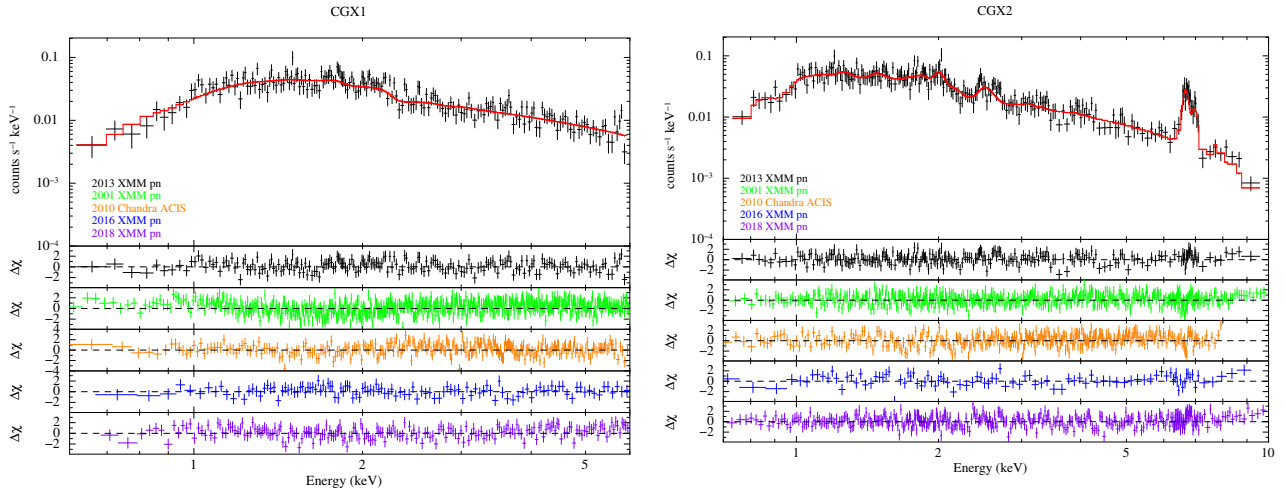
Figure 2. *Left panel* : The 0.5−6.0 keV *XMM-Newton* pn 2013 spectrum and residuals of all epochs for CGX1. All epochs spectra are fitted with a simple absorbed power law. *Right panel* : The 0.5−10.0 keV *XMM-Newton* pn 2013 spectrum and residuals of all epochs for CGX2. All epochs spectra are fitted with a model characterised by the thermal emission from shock heated material. All epochs spectra are fitted with the same model.
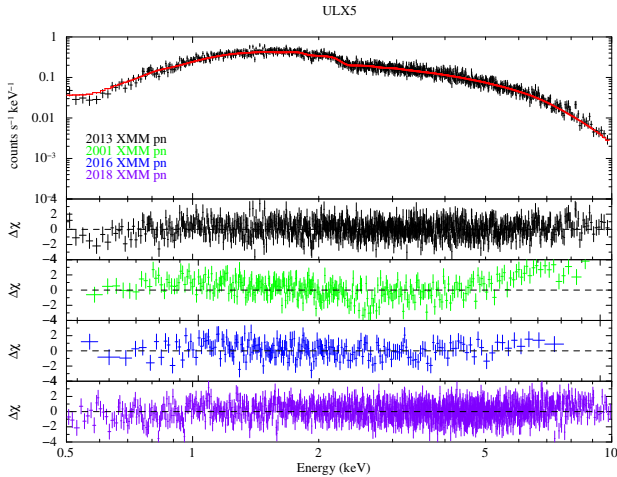
Figure 3. The 0.5−10 keV *XMM-Newton* pn 2013 spectrum and residuals for all four epochs for ULX5. All epochs spectra are fitted with DISKBB model.

Figure 4. The 0.7-8.0 keV *Chandra* spectrum of diffuse X-ray emission fitted with a model consisting of a soft component represented by APEC plus a hard component represented by Compton reflection and emission lines.

4.2 CGX2

CGX2 is known to be a young supernova remnant and the X-ray emission is interpreted as the thermal X-ray emission arising from a shock-heated plasma produced by the interaction of outflowing supernova ejecta with the circum-stellar material (CSM) (Quirola-Vásquez et al. 2019). The CGX2 is located at RA = 14^h 13^m $10^s.01$, DEC = -65° 20′ 44″.4, 25″ south of AGN. In *Chandra* ACIS image of 2010, CGX2 is neatly separated from the diffuse emission around AGN. We extracted the source spectrum by considering a circular extraction region of 2″.4 radius centred at CGX2. The background spectrum was extracted from an annular region centered at CGX2 with inner and outer radii of 5″.0 and 7″.0, respectively. The *XMM-Newton* pn spectra of different epochs were extracted using a circular extraction region of 10″ radius. The background spectra were extracted in a manner similar to that for CGX1, i.e., an annulus centred at

CGX2 with the exclusion of masked regions around CGX1 and AGN.

We find that the 0.5−10 keV *Chandra* ACIS and *XMM-Newton* pn/MOS spectra can be best−fitted with a combination of two VPSHOCK models. The VPSHOCK model characterises X-ray emission arising from a constant temperature shock-heated plasma (Borkowski et al. 2001). The best fit of the *XMM-Newton* pn spectrum for the 2013 epoch is obtained with a model consisting of two VPSHOCK components with plasma temperatures (kT) of $2.98^{+1.81}_{-0.87}$ keV and $7.89^{+0.75}_{-0.69}$ keV (see Table 2). The two plasma components can be interpreted as the forward and reverse shock emission. The two plasma emission components are absorbed with a column density (N_H) in the range of $0.23^{+0.08}_{-0.08}-0.70^{+0.08}_{-0.08} \times 10^{22}$ cm^{-2} in addition to the galactic column density of 5.6×10^{21} cm^{-2}. For simplicity, we assumed that both plasma components suffer from the same amount of absorption, and hence N_H of

both components were tied together. We find that the *XMM-Newton* pn and *Chandra* spectra of other epochs can be fitted reasonably well with the same model (see Table 2). To maintain the same baseline model with minimum free parameters, we fixed plasma temperatures to 3.0 keV and 8.0 keV, values similar to that obtained from the 2013 epoch *XMM-Newton* pn spectrum. We note that, in addition to the plasma temperature, the VPSHOCK model includes ionisation timescale $\tau = n_e t$, where n_e is the electron density and t is the time since the plasma was shocked, individual atomic abundances for various elements such as He, C, N, O, Ne, Mg, Si, S, Ar, Ca, Fe, Ni. The *Chandra* and *XMM-Newton* spectra show the presence of various emission lines, including strong Fe lines. We obtain improved spectral fits by adding multiple narrow Gaussian lines that account for broad asymmetric profiles of emission lines present at various energies in the range of 0.8 to 7.8 keV. In our best fits, most of the emission lines except Fe lines can be accounted for by using abundances fixed to Solar values. As expected, our fitted parameters are broadly consistent with those reported by Quirola-Vásquez et al. (2019), who characterised the continuum emission with the same model but convolved it with the SHELLBLUR model. The SHELLBLUR model accounts for asymmetry in emission line profiles, clearly seen in the *Chandra* grating spectra.

4.3 ULX5

The ULX5 located at RA = 14^h 12^m 39^s, DEC = -65° 23′ 34″ at the distance of 4′.5 away from AGN is clearly detected in the *XMM-Newton* pn and *NuSTAR* images. ULX5 lying in the outskirts of Circinus galaxy is known to be a variable source with X-ray luminosity in the range of 4.5 × 10^{39} to 1.8 × 10^{40} erg s^{-1} (see Walton et al. 2013; Mondal et al. 2021). We extracted *XMM-Newton* pn spectra using a circular aperture of 30″ radius. The background spectra were extracted using a source-free region in the same chip. We find that 0.5−10 keV multi-epoch *XMM-Newton* pn/MOS spectra can be best−fitted with the DISKBB model characterising emission from an accretion disk assumed to be consisting of multiple blackbody components. The spectral modelling of different epochs yields the temperature of the accretion disk in the range of 1.0 to 2.0 keV (see Table 2). The 0.5−10 keV flux and accreting disc temperature suggest ULX5 to be in a high state in the 2013 and 2018 epochs, while it appears to be in a low state during the 2001 and 2016 epochs. Figure 3 shows multi-epoch spectral fits and residuals.

4.4 Diffuse soft X-ray emission

The *Chandra* ACIS image shows extended diffuse X-ray emission around the AGN with an apparent elongation towards the north−west direction (see Figure 1). We extracted the spectrum using a polygon region such that it includes most of the extended emission and excludes AGN and X-ray point sources. We find that the 0.7−8.0 keV *Chandra* X-ray spectrum can be fitted with a model consisting of a soft component represented by the APEC model characterising the emission from hot gas, and a hard component representing the scattered emission from AGN (see Figure 4). The hard component can be described by the scattered power law component in the MYTORUS model. Our best-fitted model gives a

plasma temperature of $0.82^{+0.02}_{-0.02}$ keV and a steep power law ($\Gamma = 2.0$) emission Compton-scattered from a nearly edge-on torus ($\theta_{incl} = 80°$) with the line-of-sight column density of 10^{25} cm^{-2}, which allows no directly transmitted component in the *Chandra* energy band (see Table 2). We obtain the best fit (reduced $\chi^2 = 1.15$) by keeping the elements abundance in APEC model as a free parameter and by adding a few unresolved Gaussian emission lines at 0.74 keV, 1.3 keV and 1.8 keV. The elements abundance is only 0.2 times of the Solar value.

Our *Chandra* X-ray spectrum is similar to that reported in Arévalo et al. (2014), who analysed 0.7−8.0 keV *Chandra* spectra of different regions, i.e., ionisation cone, circumnuclear region, central annulus, large-scale extended emission, and found similar spectra for all the regions. Mingo et al. (2012) highlighted the morphological correspondence between radio lobes and diffuse extended X-ray emission at kpc-scales and favoured a scenario in which extended diffuse X-ray emission is mainly arising from the shock-heated gas produced via the interaction of the radio jet with the surrounding gas. They found that the soft X-ray spectrum can be fitted well with the APEC model yielding gas temperature (kT) of 0.74 keV and a low elements abundance of 0.15 $Z_\odot$. We note that our spectral parameters are consistent with the previous studies (e.g., Mingo et al. 2012; Arévalo et al. 2014).

4.5 Contamination model

To account for the contributions from all contaminating sources while performing broadband spectral fittings, we formulate a contamination model. We define contamination model as the sum of the models characterising contaminants (CGX1, CGX2 and extended X-ray emission), i.e., TBABS × (TBABS × PO + TBABS × VPSHOCK + TBABS × VPSHOCK + APEC + LINES). We note that the hard component of diffuse extended X-ray emission is a Compton-scattered AGN component which would be included in the physically motivated models considering the scattered emission from AGN. Hence, we do not add a scattered power law component to our contamination model. In the case of *BeppoSAX*, *Suzaku* and *AstroSat* spectral modelling, we include the contribution from ULX5, and hence, the contamination model is defined as TBABS × (TBABS × PO + TBABS × VPSHOCK + TBABS × VPSHOCK + APEC + LINES + TBABS × DISKBB). We note that, for epochs with no simultaneous *XMM-Newton* observations, we consider the fact that the multi-epoch spectra of a contaminant can be fitted with the same model and variability seen across different epochs can be accounted for by a varying normalisation (see Table 2). Thus, while modelling broadband spectra, we fixed spectral shapes and parameters of contaminants but varied their normalisations within a range observed from their multi-epoch spectral fittings. The contribution from extended diffuse X-ray emission is likely to remain constant. Hence, we keep all the spectral parameters of the soft component of the diffuse emission fixed.

5 BROADBAND X-RAY SPECTRAL MODELLING

We modelled the broadband X-ray spectra of Circinus using all ten epochs of hard X-ray observations (see Table 1). We avoid soft X-ray data points below 3.0 keV to mitigate the

effects of off-nuclear contaminating sources. The exclusion of X-ray data below 3.0 keV also brings uniformity in terms of spectral coverage for all the multi-epoch spectra, considering that only *NuSTAR* spectra covering the 3.0−79 keV energy band are available for four epochs (see Table 1). Thus, broadband spectra are limited to 3.0−79 keV whenever *NuSTAR* observations are used, even when the simultaneous *XMM-Newton* observations are available. The *BeppoSAX*, *Suzaku* and *AstroSat* spectra cover nearly 3.0−100 keV energy range.

We fitted the spectra of all ten epochs together, considering that the joint fit is useful for reducing the uncertainties in the spectral parameters and for breaking degeneracies between different parameters (Baloković et al. 2021; Saha et al. 2022). The joint fit of multi-epoch spectra can be considered equivalent to the spectrum integrated over a long period of time. Therefore, we can easily identify spectral parameters that remain constant over a long timescale. A parameter variable across different epochs can also be identified by allowing it to vary across epochs. Therefore, with the multi-epoch joint spectral modelling we aim to place better constraints on geometrical parameters such as torus average column density, covering factor and inclination angle. We also aim to probe the viability of variable line-of-sight column density ($N_{\rm H,LOS}$). To minimise the model-dependent effects, we explore three different physically-motivated models. The details of the spectral fittings with these models are given below.

5.1 Spectral modelling with MYTORUS model

The MYTORUS model considers reprocessing material distributed in a toroidal geometry with a circular cross-section and uniform density (Murphy & Yaqoob 2009). The opening angle of the torus ($\theta_{\rm tor}$) is fixed to $60°$, which gives a covering factor of ($\cos(\theta_{\rm tor})$) 0.5. The inclination angle of the torus ($\theta_{\rm incl}$), i.e., the angle between the torus symmetric axis and the line-of-sight, is a free parameter, and it can have any value in the range of $0°$ (a face-on torus) to $90°$ (an edge-on torus). The MYTORUS model considers different spectral components, i.e., AGN intrinsic emission transmitted through obscuring material, the scattered emission from the reprocessing material toward the line-of-sight, and the fluorescent emission lines, in a self-consistent manner. The three components are denoted as MYTZ (transmitted component), MYTS (Compton-scattered continuum), and MYTL (fluorescent emission lines). The MYTZ, an energy-dependent multiplicative factor applied to the intrinsic continuum, accounts for the line-of-sight obscuration. In principle, the intrinsic continuum can have any spectral shape. We assumed a power law spectral shape which is consistent with the inherent assumption of the MYTORUS model that the scattered continuum and fluorescent emission-line components are reprocessed emission of a power law continuum. The scattered component can have cutoff energy in the range of 100 keV to 500 keV. The MYTL component fits fluorescent emission lines Fe Kα and Fe Kβ at 6.4 keV and 7.06 keV, respectively.

To fit the joint spectra of different epochs, we begin with the MYTORUS model plus the contamination model. The MYTORUS model is aimed at fitting the AGN spectral components, while the contamination model accounts for the contribution from the contaminant sources (see Section 4.5). We considered the transmitted component (MYTZ) and the Compton-scattered component (MYTS). In XSPEC nota-

tion, the model can be expressed as $c_1 \times$ TBABS (MYTZ $\times$ CUTOFFPL $+ c_2 \times$ MYTS $+$ lines $+$ contamination model). First, we used the MYTORUS model in the coupled configuration by tying together various parameters (i.e., photon index, column density and normalisations) of all three components. This configuration assumes that the scattered and the emission line components result from the reprocessing of the intrinsic power law emission from a uniform torus. While performing the fit, we kept photon index (Γ), column density ($N_{\rm H}$), inclination angle ($\theta_{\rm incl}$) and normalisations as free parameters. We note that the MYTORUS model introduces a cutoff on the scattered component by using different tables with termination energies fixed to 100 keV, 160 keV, 200 keV, 300 keV, 400 keV and 500 keV. To have consistency between the scattered and the transmitted components, we used a cutoff power law for the transmitted component with cutoff energy ($E_{\rm cut}$) fixed to the termination energy of the scattered component. Also, we notice that the *NuSTAR* spectra show Ni absorption edge at 8.3 keV, which is not included in the MYTORUS scattered component. Therefore, while fitting the *NuSTAR* spectra, we added Ni edge using the ZEDGE model and kept its optical depth and normalisation as free parameters. The cross-normalisation factors between different instruments are accounted by a multiplicative factor to the cumulative model and are allowed to vary for all instruments with respect to the *XMM-Newton* data of the 2013 February 03 epoch, which is fixed to one. In Table 3, we list the cross-normalisation factors for different instruments and find them to be consistent with the values reported in the literature (e.g., Madsen et al. 2017).

To fit the multi-epoch spectra, we first assumed no variability across epochs for any of the parameters. So, all the spectral parameters of different epochs were tied together with an assumption of no intra-epoch variability in all the parameters (see case (i) in Table 3). We find that the MYTORUS model reproduces Compton hump peaking at 30 keV, but it leaves significant residuals in the soft band. The 6.4 keV emission line also shows residuals for the *XMM-Newton* data points, which can be understood due to the fact that the spectral resolution of the *XMM-Newton* (150 eV) is nearly 2.5 times better than that for *NuSTAR*, which has 400 eV spectral resolution at 6.4 keV. The addition of an unresolved emission line only to the *XMM-Newton* data provides an improved fit. In the case of *BeppoSAX*, *Suzaku*, and *AstroSat* spectral fittings, we added unresolved emission lines to the MECS, XISs and SXT spectra. The addition of unresolved emission lines at various energies ranging from 3.0 keV to 7.45 keV accounts for the residuals seen in the soft band. In general, energies and normalisations of these emission lines are consistent with the previous studies (Sambruna et al. 2001; Massaro et al. 2006; Arévalo et al. 2014), which identify them as Ar, Ca, Cr, Fe and Ni lines of different ionisations, with several of them being He-like and H-like ions. Except for Fe lines, all other emission lines are less prominent with the equivalent widths in the range of 20 eV to 150 eV and normalisations of the order of 10^{-4} to 10^{-6}.

We note that keeping all the parameters tied across epochs gives an acceptable fit with χ_r^2 (dof) = 1.123 (8107) (see case (i) in Table 3). However, as expected, the fit statistics improve slightly with χ_r^2 (dof) = 1.116 (8089) if normalisations are varied across epochs. The fit statistics show further improvement if $N_{\rm H,LOS}$ is considered as a varying parameter

Table 3. The joint fit spectral parameters using MYTORUS model

Parameters	1998-03-13 (Beppo) (1)	2001-01-07 (Beppo) (2)	2006-07-21 (Suzaku) (3)	2013-01-25 (Nu) (4)	2013-02-02 (Nu) (5)	2013-02-03 (X + Nu) (6)	2013-02-05 (Nu) (7)	2016-08-23 (X + Nu) (8)	2020-01-28 (AstroSat) (9)	2020-11-26 (Nu) (10)
Model: MYTORUS + lines + contamination										
case (i) : all parameters varied but tied across epochs										
Γ						$2.28^{+0.01}_{-0.02}$				
$N_{\rm H,LOS}$						$6.10^{+0.20}_{-0.17}$				
$\theta_{\rm incl}$						$76.9^{+0.5}_{-0.5}$				
$A_{\rm Z}\,(10^{-9})$						$1.32^{+0.11}_{-0.12}$				
$A_{\rm S}$						$1.22^{+0.10}_{-0.11}$				
$E_{\rm cut}$						160^f				
χ_r(dof)						1.123 (8107)				
$C_{\rm XMM}$						1.0^f		$0.96^{+0.01}_{-0.01}$		
$C_{\rm NuA}$				$1.30^{+0.01}_{-0.01}$	$1.23^{+0.02}_{-0.02}$	$1.23^{+0.01}_{-0.01}$	$1.19^{+0.01}_{-0.01}$	$1.34^{+0.02}_{-0.02}$		$1.20^{+0.01}_{-0.01}$
$C_{\rm NuB}$				$1.35^{+0.01}_{-0.01}$	$1.27^{+0.02}_{-0.02}$	$1.26^{+0.01}_{-0.01}$	$1.22^{+0.01}_{-0.01}$	$1.40^{+0.02}_{-0.02}$		$1.21^{+0.01}_{-0.01}$
$C_{\rm XIS0}$	$0.81^{+0.01}_{-0.01}$ (ME)	$0.77^{+0.01}_{-0.01}$ (ME)	$0.94^{+0.01}_{-0.01}$						$0.72^{+0.04}_{-0.04}$ (S)	
$C_{\rm XIS1}$			$0.96^{+0.01}_{-0.01}$							
$C_{\rm XIS2}$			$0.91^{+0.01}_{-0.01}$							
$C_{\rm XIS3}$			$0.91^{+0.01}_{-0.01}$							
$C_{\rm PIN}$	$1.18^{+0.03}_{-0.03}$ (P)	$1.03^{+0.03}_{-0.03}$ (P)	$1.45^{+0.02}_{-0.02}$						$0.91^{+0.05}_{-0.05}$ (LX)	
$C_{\rm GSO}$			$1.56^{+0.26}_{-0.26}$						$1.52^{+0.25}_{-0.25}$ (CZ)	
case (ii) : only normalisation untied across epochs										
Γ						$2.27^{+0.02}_{-0.02}$				
$N_{\rm H,LOS}$						$6.03^{+0.18}_{-0.18}$				
$\theta_{\rm incl}$						$76.7^{+0.5}_{-0.5}$				
$A_{\rm Z}\,(10^{-9})$	$1.32^{+0.18}_{-0.16}$	$1.22^{+0.22}_{-0.20}$	$1.32^{+0.12}_{-0.12}$	$1.25^{+0.13}_{-0.12}$	$1.27^{+0.14}_{-0.13}$	$1.28^{+0.12}_{-0.11}$	$1.29^{+0.14}_{-0.12}$	$1.36^{+0.14}_{-0.13}$	$1.45^{+0.42}_{-0.31}$	$1.29^{+0.13}_{-0.12}$
$A_{\rm S}$	$1.23^{+0.17}_{-0.15}$	$1.05^{+0.19}_{-0.17}$	$1.23^{+0.12}_{-0.11}$	$1.10^{+0.11}_{-0.10}$	$1.14^{+0.12}_{-0.11}$	$1.16^{+0.11}_{-0.10}$	$1.17^{+0.12}_{-0.11}$	$1.30^{+0.13}_{-0.12}$	$1.48^{+0.43}_{-0.32}$	$1.17^{+0.12}_{-0.11}$
$E_{\rm cut}$						160^f				
χ_r(dof)						1.116 (8089)				
case (iii) : only $N_{\rm H,LOS}$ untied across epochs										
Γ						$2.28^{+0.01}_{-0.01}$				
$N_{\rm H,LOS}$	$6.00^{+1.35}_{-1.34}$	$6.28^{+1.09}_{-1.17}$	$4.43^{+0.22}_{-0.32}$	$6.47^{+0.20}_{-0.19}$	$6.33^{+0.25}_{-0.20}$	$6.39^{+0.21}_{-0.20}$	$6.09^{+0.20}_{-0.20}$	$5.28^{+0.47}_{-0.18}$	$4.86^{+1.15}_{-0.84}$	$6.14^{+0.47}_{-0.16}$
$\theta_{\rm incl}$						$77.2^{+0.8}_{-0.5}$				
$A_{\rm Z}\,(10^{-9})$						$1.36^{+0.20}_{-0.11}$				
$A_{\rm S}$						$1.29^{+0.20}_{-0.10}$				
$E_{\rm cut}$						160^f				
χ_r(dof)						1.101 (8098)				
case (iv) : $N_{\rm H,LOS}$ and normalisations untied across epochs										
Γ						$2.28^{+0.01}_{-0.01}$				
$N_{\rm H,LOS}$	$6.17^{+1.36}_{-1.43}$	$6.23^{+1.17}_{-1.22}$	$4.48^{+0.22}_{-0.34}$	$6.43^{+0.21}_{-0.32}$	$6.37^{+0.32}_{-0.32}$	$6.39^{+0.22}_{-0.33}$	$5.97^{+0.28}_{-0.36}$	$5.14^{+0.38}_{-0.22}$	$5.32^{+2.80}_{-1.84}$	$6.18^{+0.19}_{-0.40}$
$\theta_{\rm incl}$						$77.1^{+0.6}_{-0.7}$				
$A_{\rm Z}\,(10^{-9})$	$1.37^{+0.13}_{-0.12}$	$1.27^{+0.20}_{-0.18}$	$1.35^{+0.03}_{-0.03}$	$1.33^{+0.04}_{-0.04}$	$1.35^{+0.08}_{-0.08}$	$1.34^{+0.03}_{-0.03}$	$1.32^{+0.07}_{-0.07}$	$1.32^{+0.07}_{-0.05}$	$1.43^{+0.62}_{-0.52}$	$1.35^{+0.04}_{-0.04}$
$A_{\rm S}$	$1.31^{+0.18}_{-0.18}$	$1.14^{+0.16}_{-0.20}$	$1.28^{+0.12}_{-0.15}$	$1.25^{+0.14}_{-0.14}$	$1.28^{+0.16}_{-0.16}$	$1.27^{+0.13}_{-0.13}$	$1.23^{+0.14}_{-0.15}$	$1.22^{+0.18}_{-0.14}$	$1.44^{+0.67}_{-0.59}$	$1.28^{+0.14}_{-0.19}$
$E_{\rm cut}$						160^f				
χ_r(dof)						1.102 (8080)				

Notes - *Beppo* : *BeppoSAX*; *X + Nu* : *XMM-Newton* plus *NuSTAR*; *Nu* : *NuSTAR*. $C_{\rm XMM}$, $C_{\rm NuA}$, $C_{\rm NuB}$, $C_{\rm XIS0}$, $C_{\rm XIS1}$, $C_{\rm XIS2}$, $C_{\rm XIS3}$, $C_{\rm PIN}$, $C_{\rm GSO}$ represent cross-normalisation factors for *XMM-Newton*, *NuSTAR* FPMA, *NuSTAR* FPMB, *Suzaku* XIS0, XIS1, XIS2, XIS3, PIN and GSO, respectively. The cross-normalisation factors for *BeppoSAX* MECS, PDS, *AstroSat* SXT, LAXPC and CZTI are indicated with 'ME', 'P', 'S', 'LX' and 'CZ', respectively. The units of column densities, inclination angle ($\theta_{\rm incl}$) and normalisations are 10^{24} cm^{-2}, degrees and erg cm^2 s^{-1} keV^{-1}, respectively. ^{f} Fixed value of a parameter.

across epochs (see case (iii) in Table 3). We note that, an equally good fit is obtained if normalisations across epochs are tied but $N_{\rm H,LOS}$ is kept variable (see case (iv) in Table 3). Therefore, our joint spectral fitting favours the variability in $N_{\rm H,LOS}$ across epochs. It is worth noting that, the fit statistics show no significant improvement if other parameters such as photon index (Γ), inclination angle ($\theta_{\rm incl}$) are kept variable across epochs. Thus, our spectral modelling with the MYTORUS model shows that, in all epochs, AGN emission can be characterised with a steep power law spectrum ($\Gamma = 2.28^{+0.01}_{-0.01}$) piercing through a Compton-thick line-of-sight column density ($N_{\rm H,LOS}$ in the range of $4.48^{+0.22}_{-0.34} \times 10^{24}$ cm^{-2} to $6.43^{+0.21}_{-0.32} \times 10^{24}$ cm^{-2}) in a nearly edge-on ($\theta_{\rm incl} = 77°$) torus. Further, we find that the transmitted component

vanishes with its normalisation nearly 10^9 times lower than that of the scattered component. The absence of the transmitted component can be ascribed to a heavily Compton-thick line-of-sight column density wherein hard X-ray spectrum (> 10 keV) is fully accounted for by the scattered component. We note that our results are consistent with Arévalo et al. (2014), who modelled $2.0 - 79$ keV combined spectra of *XMM-Newton*, *NuSTAR* spectra and *Swift*/BAT and reported a Compton scattered dominated steep power law ($\Gamma = 2.2 - 2.4$) spectrum from an obscured AGN with torus equatorial column density of $N_{\rm H} = 6-10 \times 10^{24}$ cm^{-2}.

To examine the possibility of a patchy torus in which transmitted and scattered components encounter different column densities, we performed spectral fitting by untying the column

densities of the transmitted and the scattered components. We obtained nearly the same fit statistics with nearly the same parameters, although, globally averaged column density ($N_{\rm H,avg} = 5.70^{+0.30}_{-0.30} \times 10^{24}$ cm^{-2} − 10^{25} cm^{-2}) implied from the scattered component is significantly lower than the line-of-sight column density ($N_{\rm H,LOS} \geq 10^{25}$ cm^{-2}). In fact, $N_{\rm H,LOS}$ is encountering the upper limit allowed in the MY-TORUS model, and an actual value can be even higher. A significantly higher line-of-sight column density than the global average column density indicates a patchy torus around the AGN. However, we point out that the line-of-sight column density, attaining the upper limit of its value allowed by the model, remains unconstrained. To overcome this issue, we attempted to fit our multi-epoch spectra using other models described below.

5.2 Spectral modelling with BORUS02 model

The BORUS02 model (Baloković et al. 2018) assumes uniform-density reprocessing matter having a spherical geometry with two conical polar cut-outs. The BORUS02 model consists of a Compton-scattered continuum and fluorescent emission lines. The intrinsic continuum is accounted separately by a cutoff power law multiplied by a line-of-sight absorbing column density (TBABS) and the Compton scattering losses (CABS) occurred along the line-of-sight. Unlike the MYTORUS model, this model considers covering factor (f_c) that can vary in the range of 0.1 to 1.0, corresponding to the torus opening angle ($\theta_{\rm tor}$) in $0°$ to $84°$ range. The torus inclination angle ($\theta_{\rm incl}$) varies in the range of $0°$ to $90°$. The BORUS02 model can account for a patchy environment by allowing a line-of-sight column density ($N_{\rm H,LOS}$) to be different than the average column density of the torus ($N_{\rm H,tor}$).

We fitted the joint spectra of all ten epochs using the BORUS02 model that can be expressed as $c_1 \times$ TBABS (ZT-BABS × CABS × CUTOFFPL + BORUS02 + LINES + CONTAMINATION MODEL), where BORUS02 represents a reprocessed component. The intrinsic cutoff power law includes line-of-sight absorption and losses that occurred due to Compton-scattering. While fitting the joint spectra, we allowed all the parameters (e.g., column density, spectral index, inclination angle and opening angle of the torus) to vary but tied across epochs. Similar to the MYTORUS model, we see residuals at soft energies (< 10 keV) that can be accounted for by adding narrow Gaussians for the emission lines at various energies between 3.0 to 7.5 keV.

We find that the BORUS02 model provides an acceptable fit to the multi-epoch spectra with reduced $\chi^2 = 1.138$ for 8105 dof (see case (i) in Table 4). We note that, untying normalisations across epochs renders a slight improvement in the fit statistics with reduced $\chi^2 = 1.134$ for 8096 dof. Although, keeping variable $N_{\rm H,LOS}$ across epochs gives further improvement in the fit statistics with reduced $\chi^2 = 1.117$ for 8096 dof (see case (iii) in Table 4). Notably, we obtain nearly the same fit statistics and parameters if both normalisations and $N_{\rm H,LOS}$ are kept variable across epochs (see case (iv) in Table 4). Also, untying other parameters (e.g., photon index, $\theta_{\rm tor}$, $\theta_{\rm incl}$) across epochs gives no significant improvement in the fit statistics. Thus, the best fit of multi-epoch joint spectra suggests for a variable line-of-sight column density. We note that, similar to the MYTORUS model, the BORUS02 model too shows that the multi-epoch spectra of AGN can be characterised by a steep power law ($\Gamma = 2.40^{+0.04}_{-0.02}$) emission piercing through Compton-thick line-of-sight column density of $4.19^{+0.42}_{-0.30} - 6.39^{+0.28}_{-0.25} \times 10^{24}$ cm^{-2} with a nearly edge-on torus ($\theta_{\rm incl} \simeq 80.8^{+0.1}_{-0.1}$). However, unlike the MYTORUS model, the BORUS02 model allows us to constrain the globally averaged column density ($N_{\rm H,tor} = 14.05^{+0.86}_{-0.93} \times 10^{24}$ cm^{-2}), torus opening angle ($\theta_{\rm tor}) \simeq 73°.7$ and covering factor ($f_{\rm cov} = 0.28^{+0.01}_{-0.02}$) (see Table 4). Thus, circumnuclear material in Circinus can be described as a thin torus with an opening angle of $73°.7$, rendering a relatively low covering factor of 0.28.

5.3 Spectral modelling with UXCLUMPY model

We note that both the MYTORUS and BORUS02 models consider reprocessor of uniform density, however, circumnuclear material can be clumpy (Nenkova et al. 2008). To examine the viability of clumpy circumnuclear material, we perform spectral fitting with the UXCLUMPY model (Buchner et al. 2019) which considers clumpy structure of the reprocessing matter consists of small (angle subtended at the black hole in the range $0'.1 - 1°$) spherical clouds each having constant density. The clouds are distributed in an axisymmetric geometry with a decreasing number towards the pole from the equatorial plane following a Gaussian function $N = N_0 \exp\{-(\beta/\sigma)^m\}$, where N denotes the number of clouds seen along the line-of-sight, N_0 is the number of clouds at the equatorial plane, β is the inclination angle towards the pole from the equatorial plane, σ is the angular width of the distribution (the torus scale height) and varies in the range $6° - 90°$. In addition to an axisymmetric clumpy torus, this model considers a Compton-thick reflector near the corona, which can be interpreted as part of the dust-free broad-line region or a warped disk. The clumpy reprocessing material considered in this model results in the leakage of soft photons along the Compton-thick sight lines. Similar to the other models, the UXCLUMPY model considers transmitted component, Compton-scattered component and fluorescent emission lines in a self-consistent manner. Although, unlike previous models, the UXCLUMPY model considers line-of-sight column density that can vary in the range of 10^{20} cm^{-2} to 10^{26} cm^{-2}.

We fitted the joint spectra of all ten epochs using a model defined as CONST*TBABS*(UXCLUMPY_CUTOFF + LINES + CONTAMINATION), where the UXCLUMPY_CUTOFF represents UXCLUMPY model with a high energy cutoff in the range of 60 keV to 400 keV. The constant parameter and TBABS account for the cross-normalisation factor, and galactic column density, respectively. While performing the fit, we kept all the parameters of the UXCLUMPY model free but tied across epochs. We noticed that often torus inclination angle becomes very low, resulting in an unstable fit. Therefore, we fixed the torus inclination angle to $80°$ based on the values obtained from the MYTORUS and BORUS02 models.

Similar to our previous spectral modellings, we attempted to fit the multi-epoch spectra with the UXCLUMPY model using different scenarios. The spectral fitted parameters based on the UXCLUMPY model are listed in Table 5. We plot the best−fitted joint spectra and residuals in Figure 5. We find that the best fit is achieved when both $N_{\rm H,LOS}$ and normalisations are varied across epochs (see case (iv) in Table 5). We also tried varying other parameters (e.g., pho-

Table 4. The joint fit spectral parameters using BORUS02 model

Parameters	1998-03-13 (Beppo) (1)	2001-01-07 (Beppo) (2)	2006-07-21 (Suzaku) (3)	2013-01-25 (Nu) (4)	2013-02-02 (Nu) (5)	2013-02-03 (X + Nu) (6)	2013-02-05 (Nu) (7)	2016-08-23 (X + Nu) (8)	2020-01-28 (AstroSat) (9)	2020-11-26 (Nu) (10)
Model: BORUS02 + lines + contamination										
case (i) : all parameters varied but tied across epochs										
Γ						$2.39^{+0.04}_{-0.01}$				
$N_{\rm H,LOS}$						$6.10^{+0.33}_{-0.04}$				
$N_{\rm H,tor}$						$14.05^{+0.98}_{-0.82}$				
$\theta_{\rm tor}$						$73.8^{+0.1}_{-0.1}$				
$\theta_{\rm incl}$						$80.8^{+0.1}_{-0.1}$				
$f_{\rm cov}$						$0.28^{+0.01}_{-0.01}$				
$A_{\rm Z} = A_{\rm S}$						$13.58^{+1.27}_{-1.36}$				
$E_{\rm cut}$						$108.3^{+1.2}_{-2.1}$				
χ_r(dof)						1.138 (8105)				
$C_{\rm XMM}$						1.0^{f}		$0.94^{+0.01}_{-0.01}$		
$C_{\rm NuA}$				$1.29^{+0.01}_{-0.01}$	$1.27^{+0.01}_{-0.01}$	$1.24^{+0.01}_{-0.01}$	$1.20^{+0.01}_{-0.01}$	$1.34^{+0.01}_{-0.01}$		$1.21^{+0.01}_{-0.01}$
$C_{\rm NuB}$				$1.34^{+0.01}_{-0.01}$	$1.31^{+0.01}_{-0.01}$	$1.26^{+0.01}_{-0.01}$	$1.23^{+0.01}_{-0.01}$	$1.40^{+0.01}_{-0.01}$		$1.22^{+0.01}_{-0.01}$
$C_{\rm XIS0}$	$0.84^{+0.01}_{-0.01}$ (ME)	$0.77^{+0.01}_{-0.01}$ (ME)	$0.97^{+0.01}_{-0.01}$						$0.69^{+0.05}_{-0.05}$ (S)	
$C_{\rm XIS1}$			$0.99^{+0.01}_{-0.01}$							
$C_{\rm XIS2}$			$0.93^{+0.01}_{-0.01}$							
$C_{\rm XIS3}$			$0.93^{+0.01}_{-0.01}$							
$C_{\rm PIN}$	$1.20^{+0.02}_{-0.02}$ (P)	$1.04^{+0.02}_{-0.02}$ (P)	$1.45^{+0.02}_{-0.02}$						$0.88^{+0.05}_{-0.05}$ (LX)	
$C_{\rm GSO}$			$1.52^{+0.24}_{-0.24}$						$1.55^{+0.22}_{-0.22}$ (CZ)	
case (ii) : only normalisation is untied across epochs										
Γ						$2.39^{+0.05}_{-0.02}$				
$N_{\rm H,LOS}$						$6.16^{+0.23}_{-0.16}$				
$N_{\rm H,tor}$						$14.05^{+0.91}_{-0.77}$				
$\theta_{\rm tor}$						$73.7^{+0.2}_{-0.1}$				
$\theta_{\rm incl}$						$80.8^{+0.1}_{-0.1}$				
$f_{\rm cov}$						$0.28^{+0.01}_{-0.01}$				
$A_{\rm Z} = A_{\rm S}$	$14.09^{+2.13}_{-1.41}$	$13.19^{+1.51}_{-1.00}$	$14.17^{+2.36}_{-1.57}$	$13.26^{+0.33}_{-1.40}$	$13.21^{+1.49}_{-1.49}$	$13.92^{+1.35}_{-1.35}$	$13.52^{+1.47}_{-1.47}$	$15.02^{+0.62}_{-1.57}$	$17.97^{+2.31}_{-2.00}$	$13.65^{+0.30}_{-1.75}$
$E_{\rm cut}$						$105.7^{+2.7}_{-2.2}$				
χ_r(dof)						1.134 (8096)				
case (iii) : only $N_{\rm H,LOS}$ is untied across epochs										
Γ						$2.40^{+0.02}_{-0.01}$				
$N_{\rm H,LOS}$	$5.85^{+1.76}_{-0.81}$	$5.22^{+0.90}_{-0.68}$	$4.19^{+0.16}_{-0.14}$	$6.24^{+0.18}_{-0.15}$	$6.32^{+0.19}_{-0.16}$	$6.30^{+0.26}_{-0.21}$	$6.15^{+0.20}_{-0.16}$	$5.84^{+0.17}_{-0.14}$	$5.37^{+2.66}_{-0.72}$	$6.22^{+0.13}_{-0.12}$
$N_{\rm H,tor}$						$14.05^{+0.98}_{-1.01}$				
$\theta_{\rm tor}$						$73.7^{+0.2}_{-0.1}$				
$\theta_{\rm incl}$						$80.8^{+0.2}_{-0.1}$				
$f_{\rm cov}$						$0.28^{+0.01}_{-0.01}$				
$A_{\rm Z} = A_{\rm S}$						$14.26^{+0.26}_{-1.01}$				
$E_{\rm cut}$						$110.5^{+2.9}_{-2.0}$				
χ_r(dof)						1.117 (8096)				
case (iv) : $N_{\rm H,LOS}$ and normalisations untied across epochs										
Γ						$2.40^{+0.04}_{-0.02}$				
$N_{\rm H,LOS}$	$5.87^{+1.18}_{-1.00}$	$5.15^{+1.00}_{-0.68}$	$4.19^{+0.42}_{-0.30}$	$6.24^{+0.22}_{-0.18}$	$6.39^{+0.28}_{-0.25}$	$6.38^{+0.32}_{-0.22}$	$6.13^{+0.31}_{-0.21}$	$5.89^{+0.28}_{-0.21}$	$5.69^{+0.40}_{-0.29}$	$6.28^{+0.27}_{-0.20}$
$N_{\rm H,tor}$						$14.05^{+0.86}_{-0.93}$				
$\theta_{\rm tor}$						$73.7^{+0.1}_{-0.1}$				
$\theta_{\rm incl}$						$80.8^{+0.1}_{-0.1}$				
$f_{\rm cov}$						$0.28^{+0.01}_{-0.02}$				
$A_{\rm Z} = A_{\rm S}$	$14.88^{+1.51}_{-1.44}$	$13.59^{+1.19}_{-1.13}$	$14.82^{+2.01}_{-1.71}$	$14.05^{+0.71}_{-0.74}$	$14.62^{+1.40}_{-1.58}$	$14.81^{+1.11}_{-0.77}$	$13.88^{+1.27}_{-1.63}$	$14.60^{+1.34}_{-1.62}$	$16.93^{+3.31}_{-2.84}$	$14.68^{+0.43}_{-0.96}$
$E_{\rm cut}$						$109.4^{+4.8}_{-2.2}$				
χ_r(dof)						1.117 (8087)				

Notes - The abbreviation for spectral parameters and their units are same as mentioned in Table 3.

ton index, $\sigma_{\rm tor}$, and CTKCover) but found no further significant improvement in the fit statistics. We note that similar to the MYTORUS and BORUS02 models, the spectral modelling with the UXCLUMPY too reveals a steep spectrum ($\Gamma = 2.08^{+0.01}_{-0.01}$) AGN obscured with Compton-thick column densities. The line-of-sight column density ($N_{\rm H,LOS}$) changes from $4.13^{+2.23}_{-1.07} \times 10^{24}$ cm^{-2} to $9.26^{+0.75}_{-0.53} \times 10^{24}$ cm^{-2} across epochs. A significant change in $N_{\rm H,LOS}$ from one to other epochs at various timescales is consistent with a clumpy ob-

scuring material wherein the obscuring clouds can move in or out of the line-of-sight. A detailed discussion on the implications of variable $N_{\rm H,LOS}$ is given in Section 6.

We note that the angular dispersion of clouds in the torus ($\sigma_{\rm tor}$) is nearly $7°$ (with lower limit pegging to the hard limit of $6°$), and hence, $\sigma_{\rm tor}$ parameter indicates a thin torus. However, our spectral modelling always requires an inner ring of Compton-thick material to fully account for the scattered components. The covering factor of the inner Compton-thick

Table 5. The joint fit spectral parameters using UXCLUMPY model

Parameters	1998-03-13 (Beppo) (1)	2001-01-07 (Beppo) (2)	2006-07-21 (Suzaku) (3)	2013-01-25 (Nu) (4)	2013-02-02 (Nu) (5)	2013-02-03 (X + Nu) (6)	2013-02-05 (Nu) (7)	2016-08-23 (X + Nu) (8)	2020-01-28 (AstroSat) (9)	2020-11-26 (Nu) (10)
Model: UXCLUMPY + lines + contamination										
case (i) : all parameters varied but tied across epochs										
Γ						$2.05^{+0.01}_{-0.02}$				
$N_{\rm H,LOS}$						$8.91^{+0.14}_{-0.08}$				
$\theta_{\rm incl}$						80^f				
$\sigma_{\rm tor}$						$7.0^{+0.4}_{\rm peg}$				
CTKCover						$0.32^{+0.01}_{-0.01}$				
$A_{\rm Z} = A_{\rm S}$						$0.80^{+0.01}_{-0.03}$				
$E_{\rm cut}$						$400^{\rm peg}_{-37.4}$				
χ_r(dof)						1.165 (8106)				
$C_{\rm XMM}$						1.0^f		$0.97^{+0.02}_{-0.01}$		
$C_{\rm NuA}$				$1.19^{+0.01}_{-0.01}$	$1.16^{+0.01}_{-0.02}$	$1.16^{+0.01}_{-0.01}$	$1.11^{+0.01}_{-0.01}$	$1.25^{+0.02}_{-0.02}$		$1.11^{+0.01}_{-0.01}$
$C_{\rm NuB}$				$1.24^{+0.01}_{-0.01}$	$1.20^{+0.01}_{-0.03}$	$1.19^{+0.01}_{-0.01}$	$1.14^{+0.01}_{-0.01}$	$1.30^{+0.02}_{-0.02}$		$1.12^{+0.01}_{-0.01}$
$C_{\rm XIS0}$	$0.87^{+0.02}_{-0.02}$ (ME)	$0.80^{+0.02}_{-0.02}$ (ME)	$1.04^{+0.01}_{-0.01}$						$0.73^{+0.05}_{-0.05}$ (S)	
$C_{\rm XIS1}$			$1.08^{+0.01}_{-0.01}$							
$C_{\rm XIS2}$			$1.00^{+0.01}_{-0.01}$							
$C_{\rm XIS3}$			$1.00^{+0.01}_{-0.01}$							
$C_{\rm PIN}$	$1.10^{+0.02}_{-0.02}$ (P)	$0.96^{+0.02}_{-0.04}$ (P)	$1.34^{+0.02}_{-0.02}$						$0.84^{+0.06}_{-0.06}$ (LX)	
$C_{\rm GSO}$			$1.48^{+0.24}_{-0.24}$						$1.44^{+0.24}_{-0.24}$ (CZ)	
case (ii) : only normalisation is untied across epochs										
Γ						$2.05^{+0.01}_{-0.02}$				
$N_{\rm H,LOS}$						$8.95^{+0.19}_{-0.10}$				
$\theta_{\rm incl}$						80^f				
$\sigma_{\rm tor}$						$7.0^{+0.4}_{\rm peg}$				
CTKCover						$0.32^{+0.02}_{-0.001}$				
$A_{\rm Z} = A_{\rm S}$	$0.77^{+0.01}_{-0.03}$	$0.63^{+0.01}_{-0.02}$	$0.83^{+0.01}_{-0.03}$	$0.79^{+0.03}_{-0.02}$	$0.79^{+0.01}_{-0.02}$	$0.79^{+0.02}_{-0.03}$	$0.80^{+0.02}_{-0.02}$	$0.82^{+0.02}_{-0.03}$	$0.91^{+0.06}_{-0.06}$	$0.80^{+0.02}_{-0.02}$
$E_{\rm cut}$						$400^{\rm peg}_{-22.0}$				
χ_r(dof)						1.164 (8097)				
case (iii) : only $N_{\rm H,LOS}$ is untied across epochs										
Γ						$2.06^{+0.01}_{-0.01}$				
$N_{\rm H,LOS}$	$7.84^{+0.24}_{-0.21}$	$12.01^{+0.30}_{-0.26}$	$6.97^{+0.07}_{-0.05}$	$8.84^{+0.19}_{-0.11}$	$8.95^{+0.43}_{-0.29}$	$8.99^{+0.30}_{-0.25}$	$8.59^{+0.29}_{-0.28}$	$6.54^{+0.14}_{-0.13}$	$4.46^{+1.42}_{-0.94}$	$8.84^{+0.09}_{-0.08}$
$\theta_{\rm incl}$						80^f				
$\sigma_{\rm tor}$						$7.0^{+0.2}_{\rm peg}$				
CTKCover						$0.31^{+0.005}_{-0.001}$				
$A_{\rm Z} = A_{\rm S}$						$0.80^{+0.01}_{-0.002}$				
$E_{\rm cut}$						$400^{\rm peg}_{-14.3}$				
χ_r(dof)						1.159 (8097)				
case (iv) : $N_{\rm H,LOS}$ and normalisations untied across epochs										
Γ						$2.08^{+0.01}_{-0.01}$				
$N_{\rm H,LOS}$	$6.42^{+0.38}_{-0.36}$	$4.70^{+0.46}_{-0.44}$	$4.32^{+0.04}_{-0.03}$	$8.63^{+0.18}_{-0.14}$	$8.93^{+0.24}_{-0.31}$	$9.26^{+0.75}_{-0.53}$	$8.36^{+0.81}_{-0.67}$	$5.38^{+0.21}_{-0.21}$	$4.13^{+2.23}_{-1.07}$	$8.84^{+0.16}_{-0.15}$
$\theta_{\rm incl}$						80^f				
$\sigma_{\rm tor}$						$7.1^{+0.6}_{\rm peg}$				
CTKCover						$0.33^{+0.01}_{-0.01}$				
$A_{\rm Z} = A_{\rm S}$	$0.77^{+0.02}_{-0.02}$	$0.61^{+0.02}_{-0.02}$	$0.82^{+0.04}_{-0.01}$	$0.87^{+0.02}_{-0.01}$	$0.88^{+0.02}_{-0.01}$	$0.86^{+0.02}_{-0.01}$	$0.87^{+0.02}_{-0.01}$	$0.69^{+0.02}_{-0.01}$	$0.70^{+0.27}_{-0.07}$	$0.88^{+0.01}_{-0.01}$
$E_{\rm cut}$						$400^{\rm peg}_{-17.8}$				
χ_r(dof)						1.152 (8088)				

Notes - The abbreviation for spectral parameters and their units are the same as mentioned in Table 3.

reflector (`CTKCover`) is $0.33^{+0.01}_{-0.01}$. Both `CTKCover` and $\sigma_{\rm tor}$ parameters provide constraints on the geometry of the circumnuclear material. The implications of these parameters are discussed in Section 6. We point out that our spectral parameters from the UXCLUMPY model are broadly consistent with those obtained by Buchner et al. (2019), although we find a somewhat steeper photon index and require no warm mirror component, which is a scattered component arriving to the observer without encountering heavy absorption from the torus. One of the main differences in our spectral fitting is the inclusion of the contamination model.

6 DISCUSSION

6.1 Constraints on the geometry and covering factor

With the modelling of multi-epoch spectra of Circinus, we find the evidence for reprocessing material distributed in the form of torus around AGN. The best-fitted models favour a nearly edge-on torus with an inclination angle of $77° − 81°$, which is consistent with the findings at other wavelengths. For instance, IR interferometric observations revealed a circumnuclear dusty disc component with inclination angle of $> 75°$ (see Tristram et al. 2014; Isbell et al. 2022). In sub-millimeter wavelengths, both continuum as well as CO(3-2), [C I](1-0)
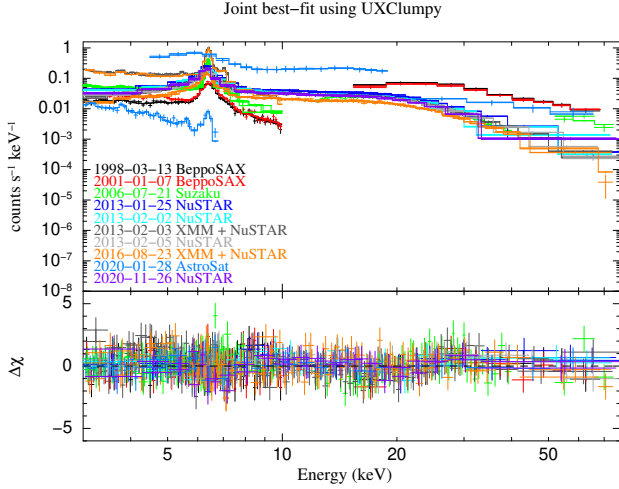
Figure 5. The multi-epoch spectra jointly fitted with UXCLUMPY model. Residuals seen around $6-7$ keV can be attributed to Fe Kα and Kβ emission lines detected with different instruments of differing energy resolution. For a better display of residuals all the spectra are rebinned with a minimum of 50 to 200 counts per bin.

emission line maps obtained with the Atacama Large Millimeter/Submillimeter Array (ALMA) showed a circumnuclear disk having the size of a few tens of parsec and inclination angle of $> 70°$. Also, H_2O maser disc is found to be edge-on with an inclination angle close to $90°$ (Greenhill et al. 2003). Therefore, a multi-phase circumnuclear material is plausibly distributed in the form of a torus that transforms into a disc at inner regions around AGN.

Further, we attempted to place constraints on the covering factor of circumnuclear reprocessing material. The MY-TORUS model yielding a good fit for the multi-epoch spectra assumes a fixed value of covering factor (f_{cov}) of 0.5. However, covering factor should not be fixed to a particular value in a prior. Therefore, we applied the BORUS02 model, which considers f_{cov} as a free parameter. We showed that our multi-epoch spectra could be jointly fitted with the BORUS02 model resulting covering factor of nearly 0.28 (see Table 4). The confidence contours between the covering factor (f_{cov}) and average column density ($N_{H,tor}$) show that both the parameters derived from the multi-epoch joint fit are well constrained (see Figure 6). Also, since keeping the covering factor a variable parameter across epochs does not improve the spectral fit, and hence, we conclude that the overall geometry of the torus remains nearly the same across all epochs.

We recall that the BORUS02 model allows us to estimate the covering factor, but it considers a uniform reprocessing material. Keeping this limitation in mind, we used the UX-CLUMPY model, which considers clumpy reprocessing material with clouds having a Gaussian distribution along the direction perpendicular to the torus equatorial plane. This model also considers an inner ring of Compton-thick material to explain Compton hump, if needed. We find that our spectra are well fitted with the UXCLUMPY model, which gives angular dispersion of nearly $7°$. Thus, a low value of angular dispersion infers a thin torus. We note that a direct comparison of covering factors obtained in the BORUS02 and the UXCLUMPY models is not possible as they assume different geometries for the reprocessing material. Although,

both models infer that the torus is likely to be thin with a relatively low covering factor. Further, we point out that an inner ring of Compton-thick reflector is needed in the UX-CLUMPY model to well describe the spectra of all epochs. The covering factor of the inner ring (CTKCover) is found to be 0.33. The inner ring may be interpreted as the wind launch site (Krolik & Begelman 1988), a puffed-up inner rim of accretion disk or a warped disk which tends to hide AGN when the torus or accretion disk is viewed edge-on, as in the case of Circinus. In a recent work, Andonie et al. (2022) suggested that the inner ring can plausibly depict the accretion disc and the BLR region.

In the literature, there have been several attempts to probe the circumnuclear material in Circinus. For instance, recently Ursini et al. (2023) performed Imaging X-ray Polarimetry Explorer (IXPE) observations and reported a significantly polarised (28 ± 7 per cent degree of polarization and a polarization angle of $18°\pm5°$) $2.0-6.0$ keV soft X-ray AGN emission mostly due to a neutral reflector. The observed polarization properties were explained by considering the reprocessing of X-ray emission from an edge$-$on uniform-density torus having the ratio of inner to outer radius $0.1-0.5$ and a half-opening angle of $45° - 55°$, which infers a covering factor of nearly 0.5, a value consistent with the MYTorus model. However, considering IR Interferometric observations of Circinus providing a direct evidence of clumpy circumnuclear environment (see Tristram et al. 2014; Stalevski et al. 2019; Isbell et al. 2022), we favour the geometrical parameters inferred from the models assuming clumpy circumnuclear material. We point out that, Uematsu et al. (2021) modelled $3-100$ keV broad-band X-ray spectrum of Circinus with a clumpy torus model and suggested a Compton-thick but geometrically thin torus with an angular width (σ) = $10.3^{+0.7}_{-0.3}$ degrees, which is consistent with our findings. Further, covering factor can be related to the accretion rate or AGN intrinsic luminosity with a trend of decreasing covering factor with the increase in accretion rate and AGN luminosity (see Buchner & Bauer 2017; Ricci et al. 2017b). The low covering factor (f_c = 0.28) found in the Circinus can be understood due to its high accretion rate, *i.e.*, L/L_{Edd} = 0.2. Circinus hosts a luminous AGN. The absorption-corrected intrinsic $2-10$ keV AGN luminosity in different epochs is found to be in the range of $2.0 - 3.7 \times 10^{42}$ erg s^{-1}, which is also consistent with the value inferred from the infrared-X-ray correlation (see, Gandhi et al. 2009; Asmus et al. 2015).

6.2 Variability in line-of-sight column density

We investigated the variability in the line-of-sight column density, which can provide a clear evidence for the clumpy circumnuclear material. From our spectral modelling, it is evident that the measured $N_{H,LOS}$ is model dependent. Therefore, for our analysis, we prefer to use $N_{H,LOS}$ measured from the UXCLUMPY model owing to the fact that both MYTorus and BORUS02 models assume a uniform-density torus. In Figure 7, we plot the line-of-sight column density ($N_{H,LOS}$) for all ten epochs using the best-fitted values obtained from the UXCLUMPY model. We find that, $N_{H,LOS}$ exhibits a significant variability on years timescales. For instance, $N_{H,LOS}$ changes from $6.42^{+0.38}_{-0.36} \times 10^{24}$ cm^{-2} $4.70^{+0.46}_{-0.44} \times 10^{24}$ cm^{-2} between 1998 March 13 to 2001 January 07, i.e., a nearly 27 per cent decrease in 3 years timescale.
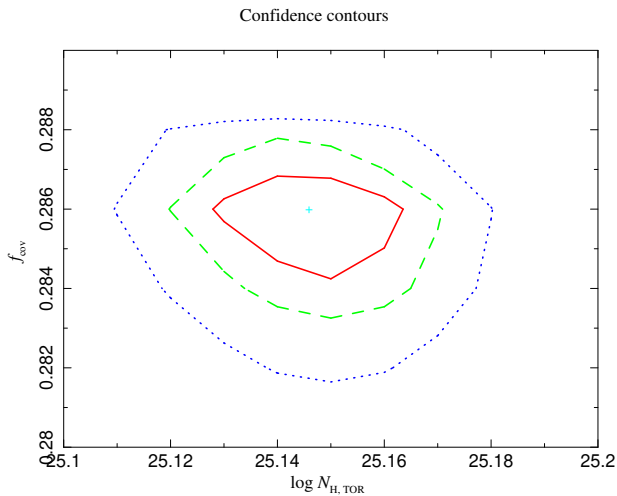
Figure 6. The confidence contours based on the joint spectral fitting with the BORUS02 model. The confidence contours from inward to outward represent 1σ, 2σ and 3σ significant level.
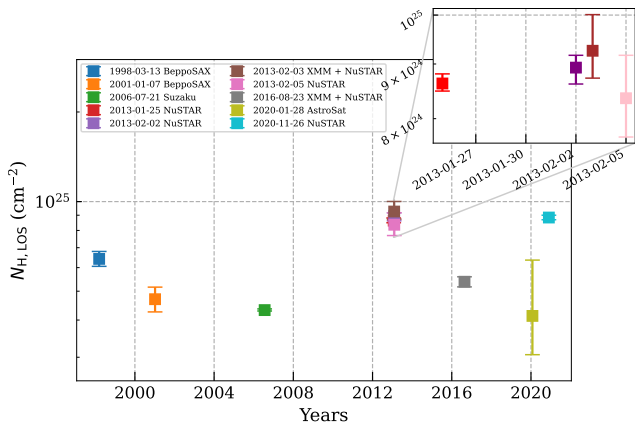
Figure 7. The plot showing line-of-sight column density ($N_{\rm H,LOS}$) variability across different epochs. The estimates of $N_{\rm H,LOS}$ are based on the best fit (case-iv) of joint spectral modelling using the UXCLUMPY model.

From 2006 July 21 to 2013 January 25, $N_{\rm H,LOS}$ becomes nearly double, which is 100 per cent increase in 6.5 years. The $N_{\rm H,LOS}$ variation on months timescales is also evident. We find that $N_{\rm H,LOS}$ changes from $4.13^{+2.23}_{-1.07} \times 10^{24}$ cm^{-2} to $8.84^{+0.16}_{-0.15} \times 10^{24}$ cm^{-2} between 2020 January 28 and 2020 November 26. The *NuSTAR* observations separated by one day to couple of weeks in 2013 allow us to probe $N_{\rm H,LOS}$ variability on shorter timescales. One of the noticeable variations can be seen between 2013 February 03 and 2013 February 05 where $N_{\rm H,LOS}$ changes from $9.26^{+0.75}_{-0.53} \times 10^{24}$ cm^{-2} to $8.36^{+0.81}_{-0.67} \times 10^{24}$ cm^{-2} in two days timescales. However, uncertainties on $N_{\rm H,LOS}$ makes this variation only tentative. On the shortest timescales of one day from 2013 February 02 to 2013 February 03, we find only a marginal change ($\Delta N_{\rm H,LOS} = 0.33 \times 10^{24}$ cm^{-2}) in the line-of-sight column density. The significance level of change in $N_{\rm H,LOS}$ is low due to relatively large uncertainties. Although, we find a clear evidence of change in $N_{\rm H,LOS}$ on months to year timescales. We note the our results on $N_{\rm H,LOS}$ variation should be treated

with caution as the influence of the variability in off-nuclear contaminating sources, albeit accounted by using contamination model, cannot be completely ruled out. We also point out that several studies in the literature have demonstrated the change in the line-of-sight column density on timescales ranging from hours to months as clouds of the clumpy material pass in and out of the observer's line of sight (see Risaliti et al. 2010; Ricci et al. 2016). Therefore, similar to other nearby CT-AGN (e.g., MRK 3; Guainazzi et al. 2016, NGC 1068; Zaino et al. 2020), our study demonstrates the plausible variability in $N_{\rm H,LOS}$ in Circinus on various timescales ranging from days to months to years.

6.3 Location of obscuring clouds

To know the location of obscuring cloud, we follow the method proposed by Risaliti et al. (2002, 2005) according to which the distance between the obscuring clouds and the SMBH can be estimated using the equation given below.

$$D_{\rm cl-BH} = 600 \, t_{100}^2 n_{10}^2 N_{\rm H,24}^{-2} R_{\rm S}$$

where $D_{\rm cl-BH}$ is the distance between the obscuring cloud and the black hole in units of parsec, t_{100} is time in units of 100 ks over which $N_{\rm H,LOS}$ variability observed, n_{10} is the cloud density in units of 10^{10} cm^{-3} and $N_{\rm H,24}$ is the change in the line-of-sight column density in units of 10^{24} cm^{-2}, and $R_{\rm S}$ is Schwarzschild radius. We caution that the aforementioned equation assumes that the change in $N_{\rm H,LOS}$ is caused due to a single cloud crossing the line-of-sight. It also assumes that the cloud is located sufficiently close to the AGN resulting into a large coverage of the X-ray emitting AGN. Thus, $N_{\rm H,LOS}$ variations are expected to occur only on timescales of a few days or even shorter. Hence, to estimate the location of obscuring cloud, we use $N_{\rm H,LOS}$ variations observed only on the short timescales of a few days to couple of weeks. For the sake of consistency with the assumption of the adopted method (see Risaliti et al. 2002, 2005), we used $N_{\rm H,LOS}$ derived from the UXCLUMPY model. We estimate cloud density as $n = |N_{\rm H,obs1} - N_{\rm H,obs2}|/d_{\rm corona}$ with an assumption that the change in $N_{\rm H,LOS}$ is due to a single cloud, where $N_{\rm H,obs1}$ and $N_{\rm H,obs2}$ are the line-of-sight column densities at two different epochs, and $d_{\rm corona}$ is the size of the corona. In general, X-ray corona size ($d_{\rm corona}$) is found to be in the range of $3R_{\rm S} - 15R_{\rm S}$ (see McHardy et al. 2005; Fabian et al. 2015; Kamraj et al. 2018). Considering $M_{\rm BH} = 1.7 \times 10^6 \, M_\odot$ (Koss et al. 2017) for Circinus, we obtained $R_{\rm S}$ ($2GM_{\rm BH}/c^2$) $= 5.04 \times 10^{11}$ cm.

Using variability in $N_{\rm H,LOS}$ measured across different timescales, we list the estimated distance between the obscuring clouds and the SMBH in Table 6 for two extreme values ($3R_{\rm S}$ and $15R_{\rm S}$) of corona size. As expected, we find that the change in $N_{\rm H,LOS}$ on the shortest timescales is associated with the obscuring clouds located closest to the AGN. For instance, $N_{\rm H,LOS}$ variability on a one-day timescale between the *NuSTAR* observations taken on 2013 February 02 and 2013 February 03, provide $0.015 - 0.38$ parsec distance range for obscuring cloud. Hence, the material responsible for the $N_{\rm H,LOS}$ variability on a one-day timescale is likely to be associated with the inner part of the torus. It is worth mentioning that, IR interferometric observations of Circinus have revealed dust emission from putative torus with a projected size of 0.2×1.1 pc disk-like geometry (see Tristram et al. 2014). Therefore,

Table 6. The estimate of distance between obscuring cloud and SMBH

Observation range	$t_{100\ \mathrm{ks}}$ (100 ks)	$\Delta N_{\mathrm{H,LOS,24}}$ (10^{24} cm^{-2})	$n_{10,\ \mathrm{3Rs}}$ (10^{10} cm^{-3})	$n_{10,\ \mathrm{15Rs}}$ (10^{10} cm^{-3})	$D_{\mathrm{cl-BH,\ 3Rs}}$ (pc)	$D_{\mathrm{cl-BH,\ 15Rs}}$ (pc)
2013-01-25 to 2013-02-02	6.81	0.30	19.87	3.97	19.93	0.79
2013-02-02 to 2013-02-03	0.94	0.33	21.85	4.36	0.38	0.015
2013-02-03 to 2013-02-05	1.80	0.90	59.60	11.90	1.40	0.056

Notes - $D_{\mathrm{cl-BH,\ 3Rs}}$ and $D_{\mathrm{cl-BH,\ 15Rs}}$ are the estimates of distance between obscuring cloud and SMBH using coronal size set equal to $3R_{\mathrm{S}}$ and $15R_{\mathrm{S}}$, respectively.

our constraints on the location of obscuring material based on the hard X-ray observations are consistent with the IR interferometric observations. Also, our estimate on the location of clouds in Circinus is similar to those reported in other nearby AGN, e.g., NGC 1068 (Zaino et al. 2020) and NGC 1358 (Marchesi et al. 2022). The $N_{\mathrm{H,LOS}}$ variability on a one-week timescale seen between 2013 January 25 and 2013 February 02 suggests the location of clouds at a distance of 0.79 to 19.93 parsec, which may be associated with the outer part of the obscuring torus. Also, we caution that the location of the obscuring material inferred in our analysis is only a characteristic due to the significant errors associated with $N_{\mathrm{H,LOS}}$.

7 SUMMARY

In this study, we present multi-epoch broadband X-ray spectral modelling of a nearby Compton-thick AGN in Circinus using all the available hard X-ray observations taken during ten different epochs in 22 years from 1998 to 2020. Six out of ten epochs of observations are from the *NuSTAR*, while the remaining four epochs of observations are from *BeppoSAX* (for two epochs), *Suzaku* and *AstroSat*. The *Chandra* and *XMM-Newton* imaging observations of higher spatial resolution reveal the existence of off-nuclear sources that contaminate hard X-ray spectra. Therefore, prior to the broadband spectral modelling, we account for the spectral shape and contribution of contaminating sources.

With an aim to constrain the geometry and structure of reprocessing material around AGN and its evolution, we performed broadband X-ray spectral modelling of all ten epochs using physically-motivated models, i.e., MYTORUS, BORUS02 and UXCLUMPY. We find that AGN is heavily obscured by Compton-thick column densities during all the epochs. MYTORUS model reveals a purely reflection-dominated spectrum with a vanishing transmitted component. The obscuring torus is found to be nearly edge-on with an inclination angle of 77°. The BORUS02 model infers a thin torus with an opening angle of nearly 73°.7, an inclination angle of 80°.8 and a low covering factor of 0.28. Interestingly, the UXCLUMPY model also suggests a thin torus with angular dispersion of obscuring cloud only 7° and an inner ring of Compton-thick material having a covering factor of 0.33. We find that varying geometrical parameters (σ_{tor}, `CTKCover`) across epochs renders no significant improvement in the fit statistics. Therefore, it does seem that the overall structure at parsec scale is likely to remain unchanged. One of the important results of our study is the tentative evidence of variable line-of-sight column density at all timescales ranging from one day to one week to a few years. The variable line-of-sight column den-

sity supports the presence of eclipsing clouds associated with the reprocessing material at sub-parsec scales.

FACILITIES

XMM-Newton, Chandra, NuSTAR, AstroSat, Suzaku and *BeppoSAX*.

DATA AVAILABILITY

The *AstroSat* data presented in this paper are publicly available at the archives maintained by the ISSDC, Bengaluru: https://astrobrowse.issdc.gov.in/astro_archive/archive/Home.jsp. The *XMM-Newton, Chandra, NuSTAR, Suzaku* and *BeppoSAX* data are publicly available from the archives of HEASARC maintained by NASA.

REFERENCES

Andonie C., Ricci C., Paltani S., Arévalo P., Treister E., Bauer F., Stalevski M., 2022, MNRAS, 511, 5768
Antia H. M., et al., 2017, ApJS, 231, 10

Antia H. M., et al., 2021, Journal of Astrophysics and Astronomy, 42, 32

Antonucci R. R. J., Miller J. S., 1985, ApJ, 297, 621

Arévalo P., et al., 2014, ApJ, 791, 81

Arnaud K. A., 1996, in Jacoby G. H., Barnes J., eds, Astronomical Society of the Pacific Conference Series Vol. 101, Astronomical Data Analysis Software and Systems V. p. 17

Asmus D., Gandhi P., Hönig S. F., Smette A., Duschl W. J., 2015, Mon. Not. R. Astron. Soc., 454, 766

Baloković M., et al., 2018, ApJ, 854, 42

Baloković M., Cabral S. E., Brenneman L., Urry C. M., 2021, ApJ, 916, 90

Bauer F. E., Brandt W. N., Sambruna R. M., Chartas G., Garmire G. P., Kaspi S., Netzer H., 2001, AJ, 122, 182

Bhalerao V., et al., 2017, Journal of Astrophysics and Astronomy, 38, 31

Bianchi S., Matt G., Fiore F., Fabian A. C., Iwasawa K., Nicastro F., 2002, A&A, 396, 793

Bianchi S., Maiolino R., Risaliti G., 2012, Advances in Astronomy, 2012, 782030

Boella G., Butler R. C., Perola G. C., Piro L., Scarsi L., Bleeker J. A. M., 1997, A&AS, 122, 299

Borkowski K. J., Lyerly W. J., Reynolds S. P., 2001, ApJ, 548, 820

Buchner J., Bauer F. E., 2017, MNRAS, 465, 4348

Buchner J., Brightman M., Nandra K., Nikutta R., Bauer F. E., 2019, A&A, 629, A16

Esposito P., Israel G. L., Milisavljevic D., Mapelli M., Zampieri L., Sidoli L., Fabbiano G., Rodríguez Castillo G. A., 2015, MNRAS, 452, 1112

Fabian A. C., Lohfink A., Kara E., Parker M. L., Vasudevan R., Reynolds C. S., 2015, MNRAS, 451, 4375

For B. Q., Koribalski B. S., Jarrett T. H., 2012, MNRAS, 425, 1934

Freeman K. C., Karlsson B., Lynga G., Burrell J. F., van Woerden H., Goss W. M., Mebold U., 1977, A&A, 55, 445

Gandhi P., Horst H., Smette A., Hönig S., Comastri A., Gilli R., Vignali C., Duschl W., 2009, Astron. Astrophys., 502, 457

Greenhill L. J., Kondratko P. T., Lovell J. E. J., Kuiper T. B. H., Moran J. M., Jauncey D. L., Baines G. P., 2003, ApJ, 582, L11

Guainazzi M., et al., 1999, MNRAS, 310, 10

Guainazzi M., et al., 2016, MNRAS, 460, 1954

Harrison F. A., et al., 2013, The Astrophysical Journal, 770, 103

Hönig S. F., 2019, ApJ, 884, 171

Hönig S. F., Kishimoto M., Antonucci R., Marconi A., Prieto M. A., Tristram K., Weigelt G., 2012, ApJ, 755, 149

Isbell J. W., et al., 2022, A&A, 663, A35

Jithesh V., Maqbool B., Misra R., T A. R., Mall G., James M., 2019, ApJ, 887, 101

Kalberla P. M. W., Burton W. B., Hartmann D., Arnal E. M., Bajaja E., Morras R., Pöppel W. G. L., 2005, A&A, 440, 775

Kamraj N., Harrison F. A., Baloković M., Lohfink A., Brightman M., 2018, ApJ, 866, 124

Kormendy J., Ho L. C., 2013, ARA&A, 51, 511

Koss M., et al., 2017, ApJ, 850, 74

Koyama K., et al., 2007, PASJ, 59, 23

Krolik J. H., Begelman M. C., 1988, ApJ, 329, 702

Leftley J. H., Tristram K. R. W., Hönig S. F., Kishimoto M., Asmus D., Gandhi P., 2018, ApJ, 862, 17

Madsen K. K., Beardmore A. P., Forster K., Guainazzi M., Marshall H. L., Miller E. D., Page K. L., Stuhlinger M., 2017, AJ, 153, 2

Marchesi S., et al., 2019, ApJ, 872, 8

Marchesi S., et al., 2022, ApJ, 935, 114

Marinucci A., Miniutti G., Bianchi S., Matt G., Risaliti G., 2013, MNRAS, 436, 2500

Massaro F., Bianchi S., Matt G., D'Onofrio E., Nicastro F., 2006, A&A, 455, 153

Matt G., et al., 1996, MNRAS, 281, L69

McHardy I. M., Gunn K. F., Uttley P., Goad M. R., 2005, MNRAS, 359, 1469

Mingo B., Hardcastle M. J., Croston J. H., Evans D. A., Kharb P., Kraft R. P., Lenc E., 2012, ApJ, 758, 95

Mitsuda K., et al., 2007, PASJ, 59, S1

Mondal S., Różańska A., Bagińska P., Markowitz A., De Marco B., 2021, A&A, 651, A54

Moorwood A. F. M., Lutz D., Oliva E., Marconi A., Netzer H., Genzel R., Sturm E., de Graauw T., 1996, A&A, 315, L109

Moran E. C., 2007, in Ho L. C., Wang J. W., eds, Astronomical Society of the Pacific Conference Series Vol. 373, The Central Engine of Active Galactic Nuclei. p. 425 (arXiv:astro-ph/0703069)

Morgan C. W., et al., 2012, ApJ, 756, 52

Murphy K. D., Yaqoob T., 2009, MNRAS, 397, 1549

Nenkova M., Sirocky M. M., Ivezić Ž., Elitzur M., 2008, ApJ, 685, 147

Netzer H., 2015, ARA&A, 53, 365

Puccetti S., Fiore F., Risaliti G., Capalbi M., Elvis M., Nicastro F., 2007, MNRAS, 377, 607

Puccetti S., et al., 2014, ApJ, 793, 26

Qiu Y., et al., 2019, ApJ, 877, 57

Quirola-Vásquez J., Bauer F. E., Dwarkadas V. V., Badenes C., Brandt W. N., Nymark T., Walton D., 2019, MNRAS, 490, 4536

Ramos Almeida C., Ricci C., 2017, Nature Astronomy, 1, 679

Ricci C., Trakhtenbrot B., 2022, arXiv e-prints, p. arXiv:2211.05132

Ricci C., et al., 2016, ApJ, 820, 5

Ricci C., et al., 2017a, ApJS, 233, 17

Ricci C., et al., 2017b, Nature, 549, 488

Risaliti G., Elvis M., Nicastro F., 2002, ApJ, 571, 234

Risaliti G., Elvis M., Fabbiano G., Baldi A., Zezas A., 2005, ApJ, 623, L93

Risaliti G., Elvis M., Bianchi S., Matt G., 2010, MNRAS, 406, L20

Rivers E., et al., 2015, ApJ, 815, 55

Saha T., Markowitz A. G., Buchner J., 2022, MNRAS, 509, 5485

Sambruna R. M., Netzer H., Kaspi S., Brandt W. N., Chartas G., Garmire G. P., Nousek J. A., Weaver K. A., 2001, ApJ, 546, L13

Schmitt H. R., Donley J. L., Antonucci R. R. J., Hutchings J. B., Kinney A. L., 2003, ApJS, 148, 327

Singh V., Shastri P., Risaliti G., 2011, A&A, 532, A84

Singh K. P., et al., 2017, Journal of Astrophysics and Astronomy, 38, 29

Stalevski M., Tristram K. R. W., Asmus D., 2019, MNRAS, 484, 3334

Swain S., Dewangan G. C., Shalima P., Tripathi P., Latha K. V. P., 2023, MNRAS,

Torricelli-Ciamponi G., Pietrini P., Risaliti G., Salvati M., 2014, MNRAS, 442, 2116

Tristram K. R. W., et al., 2007, A&A, 474, 837

Tristram K. R. W., Burtscher L., Jaffe W., Meisenheimer K., Hönig S. F., Kishimoto M., Schartmann M., Weigelt G., 2014, A&A, 563, A82

Uematsu R., Ueda Y., Tanimoto A., Kawamuro T., Setoguchi K., Ogawa S., Yamada S., Odaka H., 2021, ApJ, 913, 17

Urry C. M., Padovani P., 1995, PASP, 107, 803

Ursini F., et al., 2023, MNRAS, 519, 50

Walton D. J., et al., 2013, ApJ, 779, 148

Yang Y., Wilson A. S., Matt G., Terashima Y., Greenhill L. J., 2009, ApJ, 691, 131

Zaino A., et al., 2020, MNRAS, 492, 3872